2009

Using the Oxidation State of Iron Plagioclase to Evaluate Magma Oxygen Fugacity: A micro-XANES Study

Don Lac
University of Massachusetts Amherst

USING THE OXIDATION STATE OF IRON IN PLAGIOCLASE TO EVALUATE MAGMA OXYGEN FUGACITY: A MICRO-XANES STUDY

A Thesis Presented

by

DON LAC

Submitted to the Graduate School of the

University of Massachusetts Amherst in partial fulfillment

of the requirements for the degree of

Master of Science

September 2009

Geosciences

USING THE OXIDATION STATE OF IRON IN PLAGIOCLASE TO EVALUATE MAGMA OXYGEN FUGACITY: A MICRO-XANES STUDY

A Thesis Presented

by

DON LAC

Approved as to style and content by:

_____
Sheila Seaman, Chair

_____
Michael J. Jercinovic, Member

_____
M. Darby Dyar, Member

_____
Michael L. Williams, Department Head
Department of Geosciences

ACKNOWLEDGMENTS

I thank my advisor, Sheila Seaman, for supervising this study and for collection the microprobe analyses of plagioclase crystals. I also thank Darby Dyar for her guidance and for the Mössbauer analyses of plagioclase crystals. I am grateful to Dr. Wes Hildreth for providing plagioclase separates from Quizapu, Katmai, and Mt. St. Helens. Finally, I thank Antonio Lanzarotti of the National Synchrotron Light Source, Brookhaven National Laboratory, for the opportunity to work on beamline X26A.

ABSTRACT

USING THE OXIDATION STATE OF IRON IN PLAGIOCLASE TO EVALUATE MAGMA OXYGEN FUGACITY: A MICRO-XANES STUDY

SEPTEMBER 2009

DON LAC, B.S., SALEM STATE COLLEGE

M.S., UNIVERISTY OF MASSACHUSETTS AMHERST

The goal of this study is to explore the relationship between the oxygen fugacity of a melt and the Fe^{3+}/Fe_{Total} of plagioclase crystals produced from the melt. If the relationship between the two can be identified, the Fe^{3+}/Fe_{Total} of plagioclase crystals could be used to calculate the oxygen fugacity of the parent melt. Melt and plagioclase $X_{Fe_2O_3}/X_{FeO}$ were measured in dacitic to rhyolitic volcanic rocks from Katmai (Valley of Ten Thousand Smokes, Alaska, USA), Quizapu (Chile), and Mount St. Helens (Washington, USA), and oxygen fugacity was calculated using the empirical relationship

$$\ln(X_{Fe_2O_3}/X_{FeO}) = a\ln fO_2 + b/T + c + \sum d_i X$$

of Kress and Carmichael (1991), and the calculated fO_2 was compared to fO_2 determined using Fe-Ti oxide barometry. MicroXANES analyses were used to determine Fe^{3+}/Fe_{Total} on discrete spots on plagioclase crystals. Mössbauer measurements of plagioclase separates were used to determine bulk plagioclase Fe^{3+}/Fe_{Total} for the Quizapu and Mount St. Helens samples. The results showed that the estimated log fO_2 is at least two orders of magnitudes more oxidized for Katmai and Mount St. Helens samples and at least four magnitudes for Quizapu sample compared to fO_2 calculated on the basis of Fe-Ti oxide barometry. Five factors influence the relationship between Fe^{3+}/Fe_{Total} in plagioclase and fO_2 in the melt, including 1) $CaO/(CaO+Na_2O)$ in plagioclase, 2) H_2O concentration in the melt, 3) crystallization pressure, 4) Fe coordination in the plagioclase crystal, and 5)

crystallographic orientation. CaO/(CaO+Na_2O) ratio, Fe coordination, and crystal orientation in plagioclase crystal produce an error bar up to 30% in the microXANES $\%Fe^{3+}/Fe_{Total}$ measurement. Because the Kress and Carmichael (1991) empirical formula is based on anhydrous melt at one atmosphere, the effects of pressure and H_2O content on their empirical formula must be considered. Overall, calculation of fO_2 using the microXANES technique with the Kress and Carmichael equation may permit monitoring of small changes in fO_2 during the crystallization of single feldspar crystals.

TABLE OF CONTENTS

LIST OF TABLES

LIST OF FIGURES

CHAPTER I

OXYGEN FUGACITY AND STUDY LOCATIONS

Introduction

The study of magma chambers is one of many petrological fields of study that provide information about Earth's evolution through time. Experimental synthesizing of mineral assemblages at fixed pressures and temperatures, and spectroscopic analyses of individual minerals provide us with interpretations of magma chamber behavior that are based on models of fractionation, partial melting of source rocks, magma mixing, and/or contamination. Volcanic eruptions record the latest characteristics of a magma chamber though mineral assemblages and chemical compositions of volcanic rocks. They preserve oxygen fugacity, temperature, pressure, water fugacity, and many other magma characteristics at the time of crystallization. These observations can also be derived through calculations involving thermodynamic phase relations.

Oxygen fugacity (fO_2) exerts a strong influence on types of crystallizing minerals, on the order of crystallization, on ionic substitution within minerals, and on phase equilibria throughout the course of magma solidification. Understanding the control of fO_2 on these factors brings us closer to understanding magma behavior and evolution. Oxygen fugacity is monitored either by the Fe^{3+}/Fe^{2+} ratio in crystal-free melts, or by mineral assemblages coexisting in melts (Frost, 1991). The Fe^{3+}/Fe^{2+} ratio mirrors oxygen concentration, providing possible means of monitoring fO_2 (Sack et al., 1980; Kilinc et al., 1983; Kress & Carmicheal, 1988 & 1991). The Fe^{3+}/Fe^{2+} ratio in plagioclase and certain hydrous minerals can record fO_2 in the melt as well (Clowe et al., 1988;

Phinney, 1992; Redhammer et al., 1993; Tegner, 1997; King et al., 2000; Sugawara, 2001).

Plagioclase feldspars are one of the most abundant minerals in the Earth crust's and upper mantle. They are significant in the study of magma evolution. Iron occurs in plagioclase as a trace element, such that the iron concentration in plagioclase is dependent on the crystal structure and fO_2. Longhi et al. (1976), Phinney (1992), Tegner (1997), Sugawara (2000 & 2001), and Lungaard and Tegner (2004) showed that the Fe^{3+}/Fe^{2+} ratio in plagioclase is proportional to the Fe^{3+}/Fe^{2+} ratio in melts. Kress and Carmichael (1991) provided an empirical formula relating Fe^{3+}/Fe^{2+} ratio to fO_2. Plagioclase incorporates Fe^{3+} more readily than Fe^{2+}, as fO_2 increases and the degree to which it accepts Fe^{3+} compared to Fe^{2+} can be described by the iron partition coefficient (wt% Fe_2O_3/FeO in plagioclase / wt% Fe_2O_3/FeO in melt) (Phinney, 1992). The main contribution of Fe^{3+} and Fe^{2+} entering into plagioclase is by the $FeAl_{-1}$ substitution vector in the tetrahedral site where one Fe^{3+} enters to the plagioclase crystal structure by replacing one Al^{3+}. The Fe^{2+} can also enter the octahedral site, but in amounts too small to affect the partition coefficient (Sugawara, 2001).

Fe-Ti oxide barometry is a commonly-used technique of determining fO_2 in mineral assemblages. It provides an estimate of fO_2 at the time when oxide minerals crystallized. The goal of this study is to establish an alternative method of determining fO_2 in melts based on the Fe^{3+}/Fe_{Total} ratio in mineral phases rather than relying on the Fe-Ti oxide barometry. I chose to work with volcanic rocks, because they crystallize just prior to eruption and the magma is then avoiding any effects of high temperature diffusion of ions (Clowe et al., 1988). This paper summarizes the quantitative analysis of

plagioclase phenocrysts by using synchrotron-generated high-energy X-rays and the Fe-XANES method of analysis of Fe^{3+}/Fe_{Total} ratio in plagioclase feldspar. Samples from Quizapu Tuff (Chile), Mt. St. Helens (Washington, USA), and Katmai (Alaska, USA) were used in this study.

Background

Oxygen Fugacity

Oxygen fugacity (or oxygen potential) is a powerful mechanism for understanding crystallization of igneous and metamorphic rocks under variable pressure, temperature, and melt composition. Oxygen fugacity is defined as $fO_2 = \gamma * PO_2$ where γ is the fugacity coefficient and PO_2 is the partial pressure of oxygen. Oxygen fugacity values are shown on a logarithmic scale. Differences of a few orders of magnitude have a profound effect on magma behavior.

Iron is the fourth most abundant element in the Earth's crust. Iron occurs in its pure iron (Fe°) and in ferrous (Fe^{2+}) and ferric (Fe^{3+}) states, dependent on oxygen concentration. Therefore, it is very common in silicate and oxide minerals for the Fe^{3+}/Fe^{2+} ratio (or Fe^{3+}/Fe_{Total}) of rocks and mineral assemblage to be used as a rigorous monitor of fO_2 (Frost, 1991). However, other elements also affect oxidation fugacity. Magnesium (Mg) and titanium (Ti) are also common elements interrelating with iron that changes the stability field of the mineral. Mg can stabilize iron silicates to higher fO_2 (Frost, 1991). Ti can increase the thermostability field, and can influence fO_2 (Arima & Edgar, 1981; Frost, 1991; King et al., 1999).

In most rocks, fO_2 is monitored by mineral equilibria. These equilibria are dependent more on mineral composition than on simply the Fe^{3+}/Fe^{2+} ratio (Frost, 1991).

From mineral assemblages in the rock, thermodynamic equilibrium reactions can be written that associate $O_{2\,(gas)}$ concentration with the chemical potential (or Gibbs free energy at one molar). Reactions (1-4) are mineral reactions associating with iron oxidation and reduction:

$$2Fe^{\circ} + SiO_2 + O_2 \Rightarrow Fe_2SiO_4 \qquad \text{QIF} \quad (1)$$
Iron$_{(S)}$ Quartz Fayalite

$$3Fe_2SiO_4 + O_2 \Rightarrow 2Fe_3O_4 + 3SiO_2 \qquad \text{FMQ} \quad (2)$$
Fayalite Magnetite Quartz

$$4Fe_3O_4 + O_2 \Rightarrow 6Fe_2O_3 \qquad \text{MH} \quad (3)$$
Magnetite Hematite

$$2Ni_{(s)} + O_2 \Rightarrow 2NiO \qquad \text{NNO} \quad (4)$$
Nickel Nickel Oxide

In reaction (1), pure iron interacts with quartz and oxygen, causing the natural iron to become divalent ion (Fe^{2+}) in the mineral fayalite. As more oxygen is added to the system, both Fe^{3+} and Fe^{2+} states coexist in magnetite as a result of the decomposition of fayalite (reaction 2). At higher fO_2 in reaction (3), all of the Fe^{2+} changes to Fe^{3+}, and hematite crystallizes. The QIF, FMQ, and MN reactions are oxygen buffers in the presence of pure mineral phases, and oxygen controls the mineral equilibria. Another common oxygen buffer (4), known as the NNO buffer, lies between the MH and FMQ buffers, and is not associated with iron redox.

Oxygen fugacity values can be extracted from the equilibrium reactions (1-4) if pure phases exist at a given temperature and pressure, on the basis of the following equations:

$$\Delta G^*_{(P,T)} = \Delta G^{\circ}_{(P,T)} + RT\ln(K_{eq}) = 0 \qquad (5)$$

$$RT\ln(K_{eq}) = -\Delta G^{\circ}_{(P,T)} \qquad (6)$$

$$\ln(K_{eq}) = -\Delta G^{\circ}_{(P,T)}/RT \qquad (7)$$

The value $\Delta G^{\circ}_{(P,T)}$ is the standard Gibb's free energy. R is the gas constant (8.314472 J · K^{-1} · mol^{-1}), and K_{eq} is the equilibrium constant. For the QIF buffer, the K_{eq} can be written as

$$K_{eq} = (a_{fayalite})/[(a_{iron})^2(a_{quartz})(a_{oxygen})] \quad (8)$$

where a_i = the activity of component i. The activities of fayalite, iron, and quartz are equal to one if they are pure solid phases.

$$K_{eq} = (a_{O2})^{-1} = (fO_2/f^{\circ}O_2)^{-1} \quad (9)$$

$$\ln(fO_2) = \Delta G^{\circ}_{(P,T)}/RT \quad (10)$$

$$\Rightarrow \log(fO_2) = \Delta G^{\circ}_{(P,T)}/2.303RT \quad (11)$$

where fO_2 = the oxygen fugacity at pressure (P) and temperature (T), and $f^{\circ}O_2$ = oxygen fugacity at the standard state of 1 bar and T of interest (i.e. $f^{\circ}O_2 = 1$). The value of 2.303 is the conversion value of the natural logarithm (ln) to logarithm (log) on base 10.

Equation (11) shows that the logarithm of fO_2 is a function of temperature if pure phases are present and if $\Delta G^{\circ}_{(P,T)}$ is known. This equation provides means of solving for fO_2 with impure components in natural systems. The activities in equation (8) must be adjusted to calculate the K_{eq} (Frost, 1991).

By solving for fO_2 in the QIF, FMQ, and MH buffer reactions using equation (7), the iron equilibrium phase boundaries of pure solid phases shown in Figure 1 can be calculated (Frost, 1991). These boundary curves show iron behavior as a function of temperature and fO_2. As temperature increases, fO_2 also increases to reflect iron oxidation.

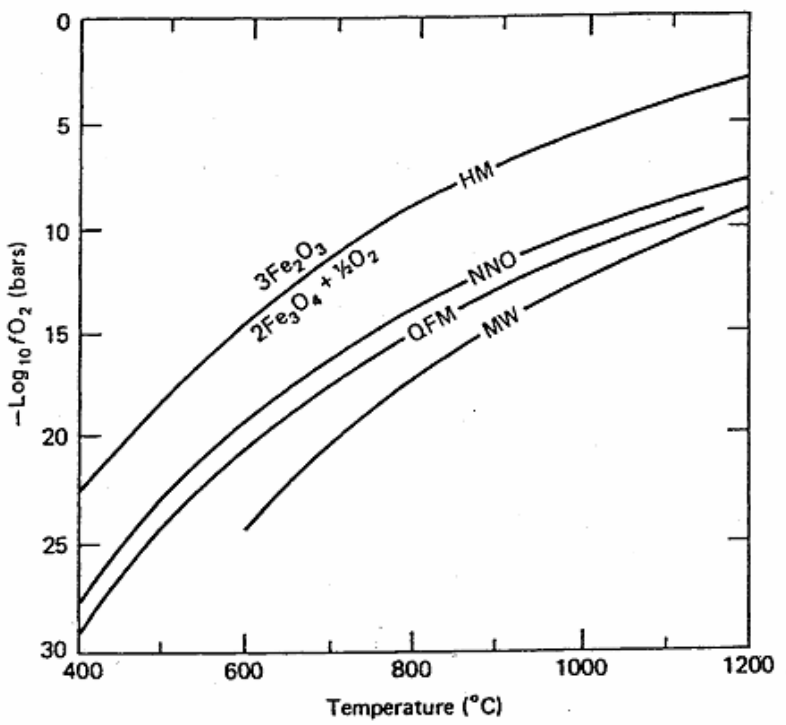

Figure 1. LogfO_2-T diagram showing the relative stabilities of the various oxidation states of iron in the system Fe-Si-O (Philpotts, 1990, p. 498)

Sack et al. (1980), Kilinc et al. (1983), and Kress & Carmicheal (1988, 1989, & 1991) developed and later revised an empirical formula relating Gibbs free energy to fO_2 derived through experimental calibrations at 1 bar over a wide range of crystalline free melt compositions. This equation relates the Fe^{3+}/Fe^{2+} ratio in the melt, fO_2, temperature, and composition of the melts. Equation (12a & b) describes iron oxidation in silicate melts.

$$2FeO_{(melt)} + 0.5O_2 = Fe_2O_{3(melt)} \quad (12a)$$

$$\text{or } FeO_{(melt)} + \tfrac{1}{4}O_2 = FeO_{1.5(melt)} \quad (12b)$$

The thermodynamic equilibrium from equation (12) is written as:

$$\Delta G^*_{(1,T)} = 0 = \underbrace{\Delta H^\circ_{(1,T)} - T\Delta S^\circ_{(1,T)}}_{=\Delta G^\circ_{(1,T)}} + RT\ln(K_{eq}) \quad (13)$$

where $\Delta H^\circ_{(1,T)}$ is the change in enthalpy; and $\Delta S^\circ_{(1,T)}$ is the change in entropy. The equilibrium constant is related to activities of the products and reactants of a reaction:

$$K_{eq} = (a_{Fe_2O_3})/[(a_{FeO})^2(fO_2)^{0.5}] \quad (14)$$

where $a_{Fe_2O_3}$ and a_{FeO} are liquid phases. The combination of (13) and (14) forms equation (15).

$$\ln(X_{Fe_2O_3}/X_{FeO}^2) = \tfrac{1}{2}\ln fO_2 - \Delta H^\circ_{(1,T)}/RT + \Delta S^\circ_{(1,T)}/R \quad (15)$$

where X is the mole fraction of component *i*. "Values a, b, c, and d_i are the experimentally calibrated constants and the summation is over melt oxide components *i* (Sack et al., 1980; Kilinc et al. 1983; Kress & Carmichael, 1991 p. 86)." For equation (15), $\ln(X_{Fe2O3}/X^2_{FeO})$ has a linear relation with $\ln fO_2$ with the slope of ½ when mixed ideally. However, Kress and Carmichael (1988 & 1989) found that the slope was consistently close to 0.3. Instead, reaction (12b) shows the slope of $\ln(X_{FeO1.5}/X_{FeO})$ vs. $\ln fO_2$ should be ¼ when mixing ideally, which is relatively close to Fudali's (1965) slope calculations varying between 0.27 and 0.16 and Kress and Carmichael (1988 & 1989)'s average slope of 0.2071. Furthermore, $\ln(X_{Fe2O3}/X_{FeO})$ produced the slope close to ½, which was within the $\ln(X_{Fe2O3}/X^2_{FeO2})$ and $\ln(_{XFeO1.5}/X_{FeO})$ experimental values (Kress & Carmichael, 1991). Therefore, an empirical formula (16) was derived for a better fit to the observations (Kress and Carmichael, 1988, 1990, & 1991).

$$\ln(X_{Fe_2O_3}/X_{FeO}) = a\ln fO_2 + b/T + c + \sum d_i X_i \quad (16)$$

The empirical formula (16) accurately predicts fO_2 in anhydrous melts within 0.5 units (Sack et al., 1980; Kilinc et al., 1983; Kress & Carmicheal, 1991). However, natural melts contain volatiles that influence viscosity, cation diffusion, electrical conductivity, and even Fe^{3+}/Fe^{2+} ratio. As water enters silicate melts, it reacts with bridging oxygen

(O^{2-}) to form two OH^- groups per broken oxygen bond (Burnham, 1975; Mysen et al., 1980). Water reacts with both nonbridging oxygen (NBO) and network modifiers (monovalent or divalent cations) to form T-OH bonds (where T can be $Si^{4+} > Al^{3+} \geq Fe^{3+}$ in tetrahedral site) and M(OH) or $M(OH)_2$ complexes (Mysen et al. 1980). Dickenson and Hess (1981 & 1986) constrained the redox of iron at constant T, P and fO_2 by changing melt compositions. They found that Al^{3+} and Fe^{3+} work as network forming (tetrahedral site) cations with monovalent or divalent network modifiers to attain charge balance in melt composition, which is similar to water reacting with the NBO. The melt composition will accept water until it reaches equilibrium. The Sykes and Kubicki (1993) model proposed that molecular water interacts with Al^{3+} to produce Al-OH bond at below 30 mol% of total water and a minor concentration of Si-OH bond. As the Al^{3+} is saturated, OH^- will complex with Fe^{3+} in order to stabilize the melt (Baker & Rutherford, 1996).

The amount of water that reacts with O^{2-} increases rapidly at low water contents due to hydroxyl groups. These are the dominating hydrogen-bearing species. At low water concentrations, the ratio between OH^- and H_2O decreases at higher (> 3 wt%) water contents (Stolper, 1982). At 4% wt. water, hydroxyl groups and water molecules are approximately equal and more water is dissolved in the melt as molecular water than as hydroxyl groups at higher water concentrations (Stolper, 1982). Furthermore, Stolper (1989) found that increase in temperature increases the proportion of dissolved water as hydroxyl groups at constant total water contents.

Moore et al. (1995) investigated the effects of dissolved water on Fe^{3+}/Fe^{2+} ratios for peralkaline rhyolite, andesite, and augite minette. Experiments were done at anhydrous and hydrous conditions. Their measurements of Fe^{3+}/Fe^{2+} ratios in anhydrous

and hydrous liquids were identical at a known temperature, pressure, and fO_2. This observation led them to conclude that the dissolution of water in silicate melts did not have an effect on the redox state of iron in silicate melts (Moore et al, 1995). However, Baker and Rutherford (1996) disagreed with the conclusions of Moore et al. (1995). Baker and Rutherford (1996) found that Fe^{3+} increases to concentration in metaluminous and peralkaline compositions with the addition of water at certain P-T-X-fO_2 conditions.

> "At NNO and high temperatures, addition of water greatly increases the Fe^{3+}/Fe^{2+} ratio in peraluminous rhyolites. The increase is linear with increasing melt hydroxyl content. At MNO, or at low temperatures, water has no effect on the Fe^{3+}/Fe^{2+} ratio in metaluminous rhyolites In peralkaline rhyolites, addition of water on redox ratio at both the MNO and NNO buffers (Baker & Rutherford, 1996 Abstract p. 2179). "

One possible reaction (17) proposed by Baker and Rutherford (1996) describes the formation of Fe^{3+} oxide from water and free Fe^{2+}. "Hydrogen in the OH^- plays a role similar to that of a charge-balancing cation for Fe^{3+} (Baker & Rutherford, 1996 p. 2184)". Reaction (17) increases the Fe^{3+} concentration depending on the availability of OH^-.

$$H_2O + Fe^{2+} = Fe_{III}(OH)^{2+} + \tfrac{1}{2}H_2 \qquad (17)$$

Gaillard et al. (2001) examined more constraints on dissolved water, Fe^{3+}/Fe^{2+} ratio, and fO_2 in silicic melts at 200 MPa and 800 to 1000°C and compared their results to Kress and Carmicheal's (1991) empirical formula. "At $fO_2 <$ NNO +1, metalumious melts have a higher calculated Fe^{3+}/Fe^{2+} ratio than from the Kress and Carmichael empirical formula, whereas at $fO_2 >$ NNO +1, the Fe^{3+}/Fe^{2+} ratios are equal or lower than calculated. The peralkaline samples show the same type of behavior (Gaillard et al., 2001 abstract p. 255)." This observation suggests that the water has the effect of oxidizing the Fe^{3+}/Fe^{2+} ratio for fO_2 below NNO +1, with which Baker and Rutherford (1996) concurred. An additional term for dissolved water needs to be added to the empirical

formula if applied to hydrous silicic melts. For fO_2 above NNO +1.5, iron oxidation is essentially controlled by the anhydrous melt composition and fO_2 (Gaillard et al., 2001). "Another implication from this study is that the iron species in the melt cannot be considered to mix ideally and that their activity coefficients depend on fO_2 and also FeO_{Total}. Significant differences exist between measured and calculated $Fe^{3+}Fe^{2+}$ ratios of silicic melts that are not all attributable to the effect of dissolved water, so that additional work is needed to describe more accurately the dependence of the Fe^{3+}/Fe^{2+} ratio on anhydrous melt composition" (Baillard et al., 2001 p. 271). Gaillard et al. (2003) extended their experiments by evaluating the activities of FeO and Fe_2O_3 in hydrous and anhydrous melts. The presence of water at low fO_2 increases the Fe^{2+} activity and decreases the Fe^{3+}, which slightly increases the Fe^{3+}/Fe^{2+} ratio overall. Their results agreed those of Gaillard et al. (2001).

Another study by Botcharnikov et al. (2005) compared water activity (aH_2O), oxidation and structural state of Fe in an iron-rich basaltic melt at T = 1200°C, P = 200 MPa, and logfO_2 ranging ΔQFM ~ +4.2 to +1 (fH_2 ~ 0.2 to 9.2 bar). "The Fe^{3+}/Fe_{Total} ratio of the glass is directly related to aH_2O in a H_2- buffered system and, consequently, to the prevailing fO_2 (through the reaction of water dissociation" (18a)) (Botcharnikov et al., 2005 p. 5071). The equation 18a can be rewritten as equation 18b where K_w is the equilibrium constant of water and then to a logarithmic form (18c)

$$H_2O = H_2 + ½O_2 \quad (18a)$$

$$K_w = fH_2O / fH_2 * fO_2^{1/2} \quad (18b)$$

$$\log(fH_2O/ fH_2) = ½\log(fO_2) + \log K_W \quad (18c)$$

where water fugacity (fH_2O) depends on aH_2O or XH_2O^n (aH_2O/ fH_2O^o; since aH_2O ~ XH_2O^n, fH_2O ~ XH_2O^n * fH_2O^o, where fH_2O^o is the fugacity of pure $H_2O_{T,P}$) (Botcharnikov et al., 2005). As Fe^{3+} content increases with increasing fO_2, the hydrogen fugacity (fH_2) and H content decrease when fH_2O (or wt% H_2O) is constant (Popp et al., 1995; and King et al., 2000).

Botcharnilov et al. (2005) showed that Fe^{3+}/Fe_{Total} ratio in basaltic melts increases nonlinearly with water wt% (Figure 2a). The Fe^{3+}/Fe_{Total} ratio increases rapidly at low water content <3 wt% due to high reaction between H_2O and Fe^{2+} ion. The reaction gradually decreases at higher water content. This supports Baker and Rutherford's (1996) conclusions. At constant water concentration and K_w, fH_2 is the controlling factor on fO_2 as shown by formulas (18 b & c). Then by the oxidation-dehydrogenation equilibrium reaction (19) in the amphibole crystal structure, the Fe^{3+}/Fe^{2+} ratio is controlled by T, P, and fH_2, which correlates Fe^{3+}/Fe^{2+} ratio back to fO_2 by the dissociation of water (18a) (Popp et al., 1995; King et al., 2000; and Botcharnikov et al., 2005).

$$Fe^{2+} + OH^- = Fe^{3+} O^{2-} + \tfrac{1}{2}H_2 \qquad (19)$$

Figure 2b shows the relationship between the X_{H2O}^{fluid}/ fH_2O and Fe^{3+}/Fe_{Total} ratio from the Botcharnilov et al. (2005) measured data. At constant wt% H_2O, Fe^{3+}/Fe_{Total} ratio increases with decreasing fH_2. Therefore, the increase of Fe^{3+}/Fe^{2+} ratio decreases the fH_2 and increases fO_2 linearly at a relatively constant T, P, and aH_2O under closed system conditions. This agrees with the dehydrogenation reaction for amphibole. However, H_2 can diffuse out of the magma chamber and that loss of H must be taken into consideration when evaluating natural silicate melts.

> "Overall, fO_2 remains the most important factor controlling the oxidation state of iron in silicate melts; whereas the presence of water is a chemical component of the melt at constant T, P, and fO_2 has a small and insignificant influence on the Fe^{3+}/Fe_{Total} ratios. However, it must be noted that the presence of water in H_2-buffered fluid saturated system is indeed important (i.e. more water generated at high fH_2 than at low fH_2) since aH_2O controls the redox state of the system and, hence, the Fe^{3+}/Fe^{2+} ratio of the silicate melt (Botcharnikov et al., 2005 pp. 5082-5083)."

Plagioclase as a Monitor of Oxygen Fugacity

Plagioclase is a ubiquitous mineral in igneous rocks, crystallizing over a wide temperature range, and providing a wealth of information about igneous processes. The chemical formula of feldspar is MT_4O_8, where M represents cations in the octahedral sites (e.g. by Ca and Na), and T is the tetrahedral cations (Si and Al). Plagioclase has two end members, anorthite and albite. Anorthite ($CaAl_2Si_2O_8$) is triclinic, whereas albite ($NaAlSi_3O_8$) is monoclinic at high temperature, and becomes triclinic at lower temperature (Griffin, 1992). The plagioclase composition (An-content) can be explained by a simple ionic substitution (20), which depends on the in-situ melt composition where the crystal crystallized.

$$^{VI}Na^{1+} + {}^{IV}Si^{4+} = {}^{VI}Ca^{2+} + {}^{IV}Al^{3+} \quad (20)$$

$$^{IV}Al^{3+} = {}^{IV}Fe^{3+} \quad (21)$$

Iron occurs as a trace element in plagioclase. It is common for Fe^{3+} to substitute for Al^{3+} in the tetrahedral site (21) (Smith, 1974). Hofmeister and Rossman (1984) found that Fe^{3+}/Fe_{total} ratio in plagioclase increases with increasing anorthite (An) content, because more Fe^{3+} is incorporated into the structure by substitution (21). Therefore, the FeO_{total} in plagioclase decreases with decreasing An content. The case studied by Tegner (1997) in the Skaergaard intrusion, however showed an inverse correlation between FeO

a.

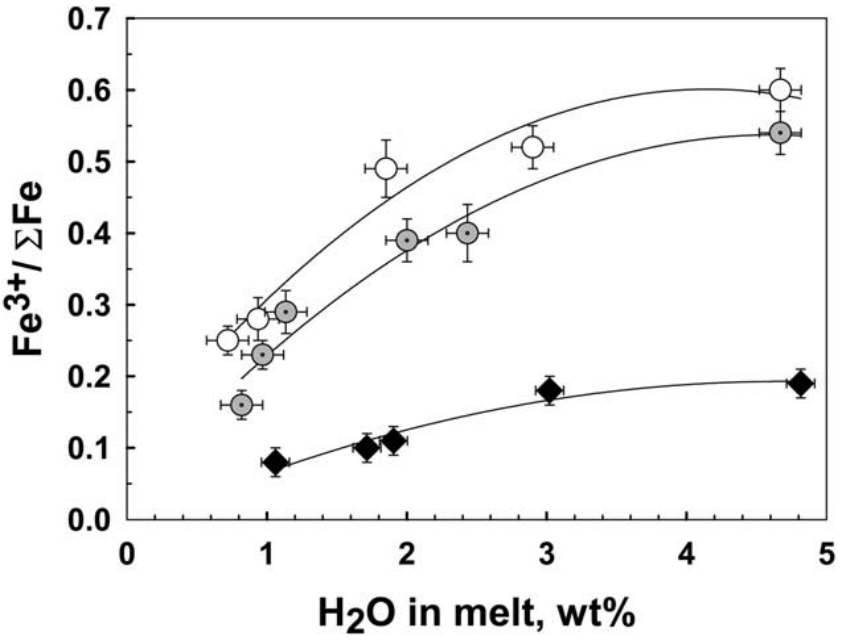

b.

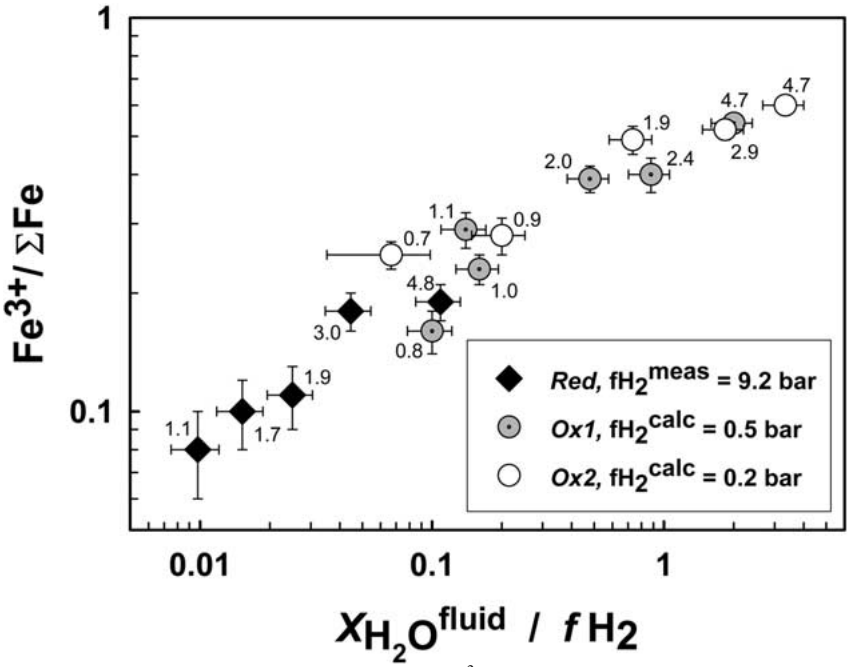

Figure 2. Relationship between $\%Fe^{3+}$ and H_2O in the basaltic melt. a. The oxidation state of Fe vs. H_2O content of basaltic glasses. Solid lines represent second order polynomials for each set of data points. b. The measured Fe^{3+}/Fe_{Total} ratio at the controlled fH_2 and wt% H_2O. Note that all data lie on a single trend (within error bars) independent of H_2O content (Botcharnikov et al., 2005, p.5080 and p. 5082).

and An content, indicating that An content was less dependent on fO_2 and mainly dependent on fractionation as Skaergaard magma evolved. Lundgaard and Tegner (2004) calculated the partition coefficients for Fe_2O_3 and FeO between plagioclase and liquid as a function of An content. The relationship is indeed apparent for partition coefficients for Fe_2O_3 in tholeiite and FeTi-tholeiite liquids with less than 60 wt% SiO_2. For calc-alkaline and alkaline liquids, the partition coefficient for Fe_2O_3 does not vary systematically with An content. Therefore, plagioclase composition is not a first-order factor controlling the partitioning of Fe_2O_3 into plagioclase (Lundgaard & Tegner, 2004).

Fe^{2+} and Mg^{2+} can enter either the M or T sites as $(Fe,Mg)Al_2Si_2O_8$ or $Ca(Fe,Mg)Si_3O_8$, respectively (Sugawara, 2001). The substitution of Fe^{2+} in the T site,

$$^{IV}Al^{3+} + {}^{IV}Al^{3+} = {}^{IV}Fe^{2+} + {}^{IV}Si^{4+} \quad (22)$$

and

$$^{IV}Al^{3+} + {}^{IV}Al^{3+} = {}^{IV}Mg^{2+} + {}^{IV}Si^{4+} \quad (23)$$

can be explained by exchange between the anorthite end member structures of ($CaAl_2Si_2O_8$) and $Ca(Fe,Mg)Si_3O_8$ (Sugawara, 2001). Longhi et al. (1976) determined that the combined Fe^{2+} and Mg held <10% in the M site. Therefore, Fe^{3+}, Fe^{2+}, and Mg in plagioclase are predominantly tetrahedrally coordinated, defined by substitutions (20-21) (Sugawara, 2000 & 2001).

One hypothesis of this study is that Fe^{3+}/Fe_{Total} ratio in plagioclase is proportional to Fe^{3+}/Fe_{Total} in the melts from which the plagioclase crystallizes. That proportion can be defined by a partition coefficient. Phinney (1992) found that the partition coefficient (D) for FeO_{Total} between calcic plagioclase (>An_{70}) and tholetiitic basalt changes very little (from 0.030 to 0.044) at low fO_2 (iron-wustite (IW) buffer), and at the fayalite-magnetite-quartz buffer (FMQ). However, D increases rapidly above the FMQ buffer to

0.14 at the magnetite-hematite (HM) buffer and 0.36 in air. An increase of D for FeO_{Total} indicates that nearly all of the iron is in the Fe^{2+} state at fO_2 below FMQ with very little change at or below the IW buffer. The Fe^{3+}/Fe_{Total} ratio in the melt increases rapidly above FMQ, causing more iron to enter the plagioclase, which accepts Fe^{3+} more readily than Fe^{2+}.

Sugawara (2001) provided thermodynamic models revised from his previous paper (Sugawara, 2000) for Fe^{3+}, Fe^{2+}, and Mg partitioning between plagioclase and silica melts, plagioclase-clinopyroxene, and plagioclase-spinel. From his algorithm, Fe^{3+}/Fe^{2+} ratio in plagioclase can be used to solve for the Fe^{3+}/Fe_{Total} ratio in melts, which is then used to solve for fO_2 by using Kress and Carmichael's (1991) revised formula (16). In 2004, Lundgaard & Tegner used Sugawara's algorithm to separate the Fe_2O_3 and FeO partition coefficients between plagioclase and melts for 23 previously published experimental studies. They conclude that calculated D_{Fe2O3} and D_{FeO} behave independently of fO_2 and plagioclase composition, and suggested that D_{FeOT} is proportional to D_{Fe2O3} and $D_{FeO.}$ Also, the positive correlation of SiO_2 in the melt rather than plagioclase composition with Fe_2O_3 and FeO is the first order influence on fO_2. They also concluded that tholeiitic basalts with less than 52% SiO_2 can be used to calculate the magma fO_2 if An content, $FeO_{Total,}$ and Fe^{3+}/Fe_{Total} ratio in plagioclase are known. For alkaline and sub-alkaline composition, The D_{Fe2O3} and D_{FeO} between melts and plagioclase can be determined from

$$\ln(D) = a + \sum b_i * m_i \qquad (24)$$

(Lundgaard & Tegner, 2004), where a and b_i are regression coefficients, and m_i is oxide

wt.% of the melt components. By substituting equation (24) into (25), X_{Fe2O3}/X_{FeO} in the melt can be calculated if the iron partitioning in plagioclase is known.

$$D_{Fe2O3}/D_{FeO} = (\text{wt.\% } Fe_2O_3/\text{wt.\% FeO})^{pl} / (\text{wt.\% } Fe_2O_3/\text{wt.\% FeO})^{melt} \qquad (25)$$

	Sub-alkaline			Alkaline	
	ln(DFe2O3)	ln(DFeO)		ln(DFe2O3)	ln(DFeO)
SiO2	0.0167	0.00298		0.0176	0.0655
TiO2	-0.0578	-0.0201		-0.0509	0.0205
Al2O3	-0.0394	-0.0589		-0.0395	-0.0155
FeO*	-0.0779	-0.0559		-0.107	0.0115
MgO	-0.0295	-0.107		-0.0872	-0.0363
CaO	-0.000558	-0.00484		-0.0252	0.1
Na2O	-0.0292	-0.14		-0.114	0.0122
K2O	0.13	-0.043		0.053	0.0642
a	-0.211	-1.555		0.98	-8.263

Table 1. Multiple regression coefficients b_i of Eq. (24) for sub-alkaline and alkaline compositions (Lundgaard and Tegner, 2004 p.477)

Geologic Background of Samples Used in This Study

1. Plagioclase crystals from three recent volcanic eruptions were used in this study. Plagioclase from Katmai, Alaska (Valley of Ten Thousand Smokes), Quizapu, Chili, and Mt. St. Helens, U.S.A. were provided by Dr. Wes Hildreth, and are the focus of this study.
2. Many workers built the existing body of data on the Katmai, Quizapu, and Mt. St. Helens eruptions. Their work provides insight into the given temperature, pressure, water content, and fO_2 of the magma, which direct affect the Fe^{3+}/Fe^{2+} ratio. Generally, temperature and fO_2 are obtained by measuring the Fe-Ti oxide equilibrium in the mineral assemblage of the samples. Pressures are defined by laboratory experiments that replicate the mineral stability field and water content at liquidus temperatures and fO_2. Therefore, the geological background of these

sites are reviewed here to provide a better understanding of how these constraints influenced the Fe^{3+}/Fe^{2+} ratio of plagioclase and the melt.

Valley of Ten Thousand Smokes (VTTS), Alaska

History of Eruption

A volcanic eruption at Novarupta in the Valley of Ten Thousand Smokes (VTTS) on June 6, 1912 produced the most voluminous debris of the twentieth century. It produced a 120 m^3 ash-flow sheet and ~ 15 km^3 of magma flow (Figure 3). The ash extends through Katmai Pass into Mageik Creek (Hildreth & Fierstein, 2000). The eruption lasted for 60 hours, and caused the collapse of the Mt. Katmai caldera10 km east of Novarupta. Andecitic-dacitic magmas originated under Mt. Katmai and migrated to Novarupta (Hildreth, 1987; Fierstein & Hildreth, 2000; Coombs & Gardner, 2001; Hammer et al., 2002).

The plinian tephra is divided into episodes I, II, and III containing A, C-D, and F-G layers, respectively (Figure 4) (Curtis, 1968; Hildreth, 1983; Adams et al., 2006). They were later interpreted by Hildreth (1983), based on observations by people on the steamer *Dora* at Shelikof Strait, and the records at Kodiak during the 60 hours long eruption (Hildreth, 1983). Layers B, E, and H were deposited between these episodes as debris that settled during the lull after each episode.

In the early stages of the eruption, a plinian outburst of tephra carried high silica-rich, phenocryst-poor, and 5-10% lithic ejecta that eventually became the basal depositional layer known as layer A. It is poorly sorted. More distal deposits are well sorted. These deposits have been found on the Pacific slope and Mageik Creek (shaded

area towards Observation Mountain on Figure 3). The air-fall segregated into finer grained deposits, which produced a very fine-grained, rhyolitic layer in the lower VTTS. Layer A was adjacent to the ash-flow sheet indicating that Layer A must have preceded or coincided with the ash-flow sheets on the same day (Hildreth, 1983).

Roughly 50% of the ash-flow sheet volume contained up to 98% rhyolitic composition (77-78% SiO_2) with 1-3% unzoned phenocrysts of plagioclase (An_{23-30}), quartz, pyroxene (En_{49-52}), and magnetite (Hildreth, 1983; Coombs & Gardner, 2001). Layer A and rhyolitic tuff extend and thin out as far as 18 km into Three Fork and Ukak River. Eventually the rhyolite gradually grades to dacite with andesitic and banded pumice that contained 30-50% phenocrysts (Hildreth, 1983; Fierstein & Hildreth, 1992; Coombs & Gardner, 2001). Plagioclase phenocrysts are strongly zoned in the dacites (An_{34-71}) and andesites (An_{35-83}), in which both normal and reverse zoning occur (Hildreth, 1983). These new simultaneously erupting magmas were hotter, more viscous, and produced a substantial volume of welded tuff. They were exposed along the vent towards the upper central VTTS, upper Knife Creek, and upper River Lethe and are overlain by thick beds of rhyolitic tuff (Figure 4). The andesitic-rich tuff found within 4-5 km near-vent area, which indicates that the andecitic ejecta was a product of a low fountaining eruption. This contributed to a pyroclastic flow instead of a Plinian column (Hildreth, 1983).

Curtis (1968) found layer B in the northeastern side of the Knife Creek arm of the upper VTTS, tracing the ash-flow sheet to elevations of 300-400 m higher. However, Hildreth (1983) said layer B (known as Feather Edge) was a fine-grained continuation of Layer A. It is largely rhyolitic, poorly sorted, pink to terra-cotta ash with 2-5% of each

phenocrysts and lithics with some additional pumice lappilli. Hildreth pointed out that layer B was deposited by the feather edge of the main rhyolite-rich ash flow. This was not noticeable in the upper VTTS region due to the andesite-dacite pumice overlying the rhyolite tuff. The 2-10 cm exposed wedge layers of pink vitric rhyolitic ash were deposited in between overlying layer A and capped by Layer C on the south of Mt. Katmai, on Broken Mountain, and on the steep slope of the Buttress Range. These features are associated with Layer B, especially at Buttress Range, because it is very similar to the Knife Creek outcrop.

Episodes II and III were the last two Plinian tephra after the ash-flow sheet deposited dacite and several andesite-rich layers in episode III (Figure 4) (Hildreth, 1983; Fierstein & Hildreth, 1992). Adams et al. (2006) studied the density, bubble size distribution, and bubble wall size. Densities of two deposits linearly increase from layers C-F exponentially through layer G. Clasts have very thin walls and relatively uniform bubbles in layer C. Layer D surpassed the other layers by having larger and more uniform bubbles, as well as the thinnest wall structure. Layer F contained more elongated vesicles between fine and intermediate bubbles. Overall, Layer G had the thickest wall structure and increasing abundances of small vesicles enter in between larger bubbles.

Layers E and H represent “quiet” zones between episodes. They are characterized by thin beds of sandy to silty ashes. Layer E was deposited by the regional dust cloud produced by the ash flow. It has a uniform thickness throughout the VTTS and is mainly dacitic with minor vitric dust. Layer H is predominantly crystal-depleted vitric ash from Layer G (Hildreth, 1983; Fierstein & Hildreth, 1992).

Eruption Conditions

Hildreth (1983) estimated the temperature and fO_2 of the magma by using the titanomagnetite-ilmenite equilibrium. Temperatures of rhyolite were 805-850°C, dacite was 855-955°C, and andesite was 955-990°C (Figure 4: modified from Hammer et al. (2002), p. 145). The fO_2 are bound by Ni-NiO buffer 0 to +2, where rhyolite is NNO 0 to +1 ($\log fO_2$ -13.7 and -12); dacite is NNO +1 ±0.1 ($\log fO_2$ -12 to -10); and andesite is NNO +1 (above $\log fO_2$ -10.1) (Hildreth, 1983; Hammer et al., 2002).
Lowenstern (1993) measured the water concentrations in episodes I and II by using FTIR spectrometry. He used melt inclusions in quartz phenocryts in rhyolitic ejecta and found 3.5-4.5% H_2O (average ~4%) at the equilibrated pressure of ~100 MPa. Melt inclusions from three plagioclase phenocrysts in layer C ranged from 2.2-3.1% (average 2.8%) H_2O. CO_2 is too low for detection (below 50ppm) in melt inclusions of rhyolitic and dacitic magmas. This indicates that the rhyolitic magma was highly saturated in H_2O.

In 2001, Coombs and Gardner determined phase equilibria for Katmai rhyolite at the NNO oxygen buffer and under water-saturated (i.e. $P_{H2O}=P_{Total}$). The pressure range from the plagioclase and orthopyroxene stability field further restricted those conditions above 70 MPa at 800°C and below 40 MPa at 840°C. Experiments below those conditions contained significantly more crystals than the natural pumice. Based on the pressure (40-100 MPa), the density of the crustal rocks, and $P_{H20} = 0.9P_{Total}$, Coombs and Gardner (2001) estimated that the rhyolitic magma should record a depth of 1.8-4.4 km. However, there is no evidence of rhyolite at >4 km (100 MPa), because the crystals preserved are all in equilibrium with low pressure melt and none contain high pressure melt inclusions (Eichelberger & Izvekov, 2000; Hammer et al., 2002 p. 159).

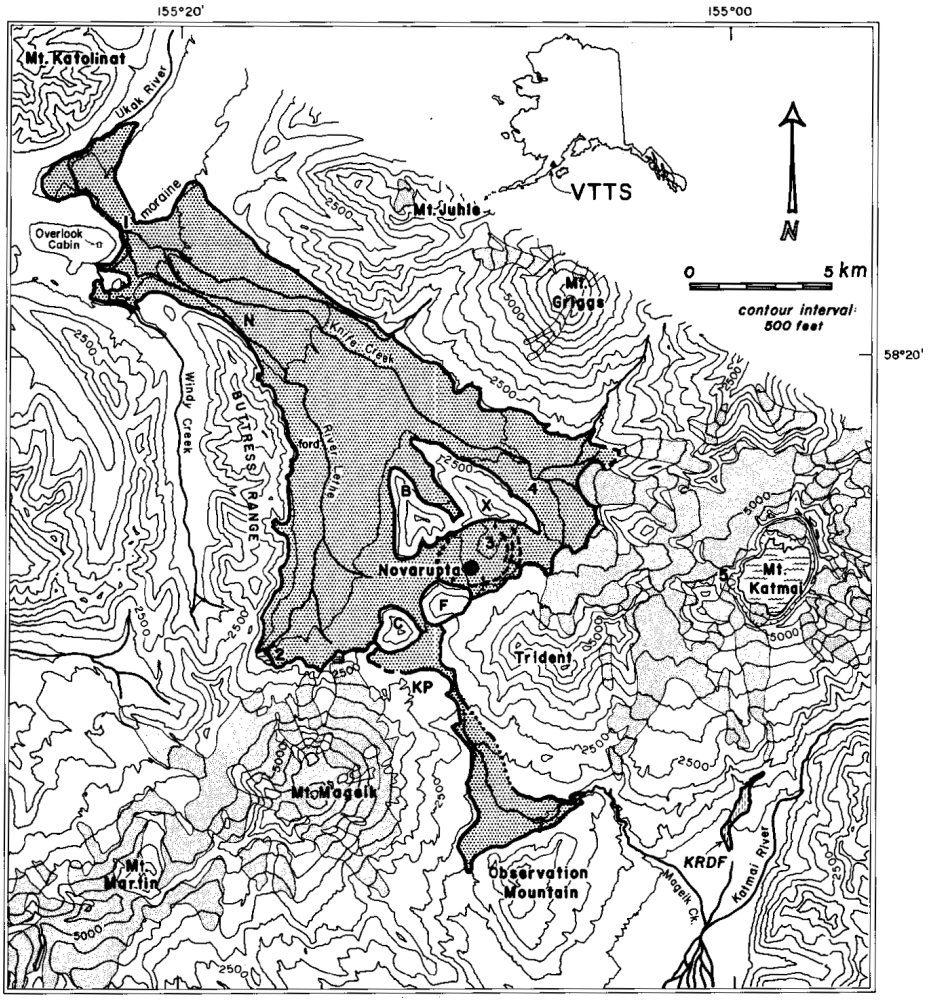

Figure 3. Topographic map of VTTS, Alaska (Hildreth and Fierstein, 1987, p. 426)

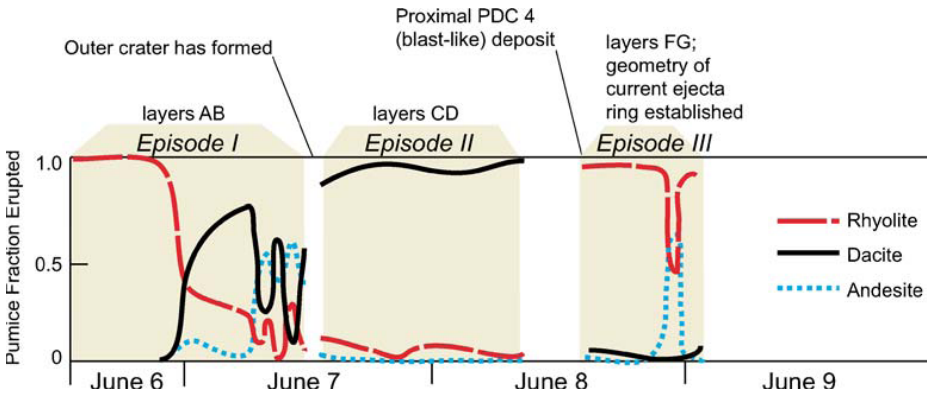

Figure 4. Eruption of 1912 at Novarupta three episodes. It shows layers within each episode and dominating composition that erupt with time. Layer E is between episode II and III. Layer H is the final deposit settling after layer G (Adams et al., 2006, p. 190).

Hammer et al. (2002) performed experiments on andesitic and dacitic magmas at H_2O saturation to constrain magma storage condition prior to the 1912 eruption. Andesitic magma was stored at ~950 °C /100 MPa to 960 °C/75 MPa with fO_2~ NNO +1.1 ($\log fO_2$ -9.85 to -9.91), which corresponds to 2.8-3.8 km. Dacitic magma was stored at ~ 850°C/50MPa to 880°C/25MPa with fO_2~ NNO +1.1 ($\log fO_2$ -11.7 to -11.4), which gives estimated depth of 0.9-1.9 km. Figure 5 shows the T-fO_2 measurements based on the Fe-Ti oxides coexisting in glass. This means that the dacitic magma may have overlain the andesitic magma under Mt. Katmai. Based on these depth estimations, andesitic-dacitic magmas should be laterally positioned relative to rhyolitic magma instead of vertically if all magmas were H_2O-saturated (Figure 6 a & b). If the andesitic-dacitic magmas were H_2O-undersaturated (where X_{H2O}^{fliud}= 0.5) or saturated with CO_2-bearing phases, the depth estimates will be ~5.7 km or ~150 MPa and ~4.9 km or ~130 MPa for andesite and dacite, respectively (Hammer et al., 2002). Hildreth & Fierstein (2000) proposed a similar model as Hammer et al. (2002) with the rhyolite vertically positioned above dacite and andesite, all being underneath Mt. Katmai (Figure 6c) when water was undersaturated in the magma.

In this study, Fe^{3+}/Fe_{Total} ratio in plagioclase crystals from VTTS, Quizapu, and MSH are measured by Fe-XANES and Mössbauer methods and are used to calculate fO_2 in the melt from Kress and Carmichael (1991) empirical formula (16). The calculated fO_2 is compared to the Fe-Ti oxide barometry value. Variations between the calculated fO_2 and Fe-Ti oxide barometry value are possibly associated with water content, pressure, mineral compositions, and magma conditions. By understanding VTTS, Quizapu, and

MSH eruption history and conditions, calculated fO_2 can achieve better estimations compared to the Fe-Ti oxide barometry value.

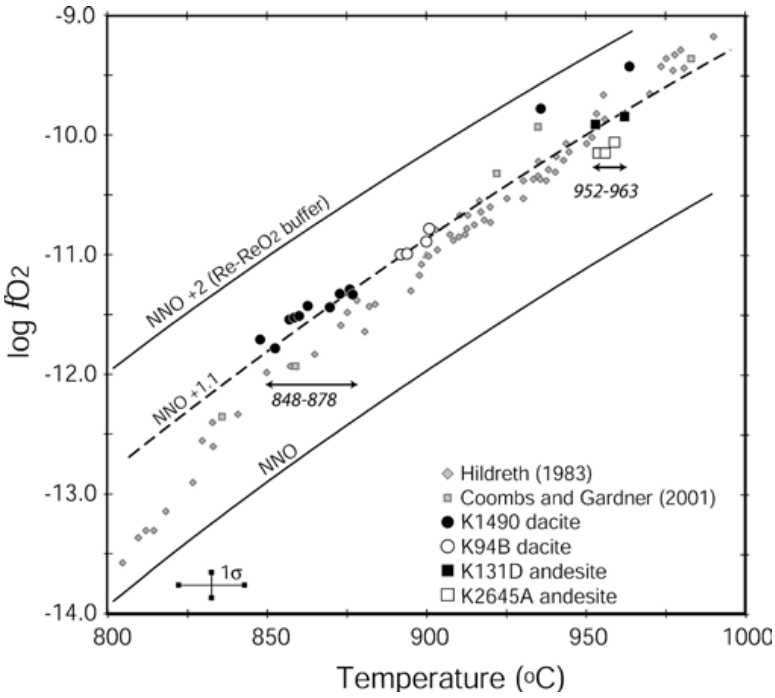

Figure 5. Temperature and Oxygen Fugacity Relationship by Fe-Ti Oxide Barometry from Novarupta Eruption of 1912 (Hammer et al., 2002, p.145).

Quizapu, Chilies

History of the Eruption

In 1846, the first eruption at Quizapu occurred north of Cerro Azul flank, marking the beginning of the Volcán Quizapu (Figure 7). An estimated 5 km^3 of dacitic (67-68% SiO_2) lava flowed out, covering an area of 50.4 km^2. Starting from 1907 to the1932 eruption, frequent plumes and ash clouds were seen over Quizapu that accumulated >50 m of black scoria at the vent wall as a result of mostly phreatic and sometime fumarolic activity (Hildreth & Drake, 1992). On the morning of April 10, 1932, a plinian eruption began that did not end until the morning of the 11^{th}, accumulating ~ 4 km^3 of dacitic

a. All Magmas H_2O-saturated, stored beneath Katmai

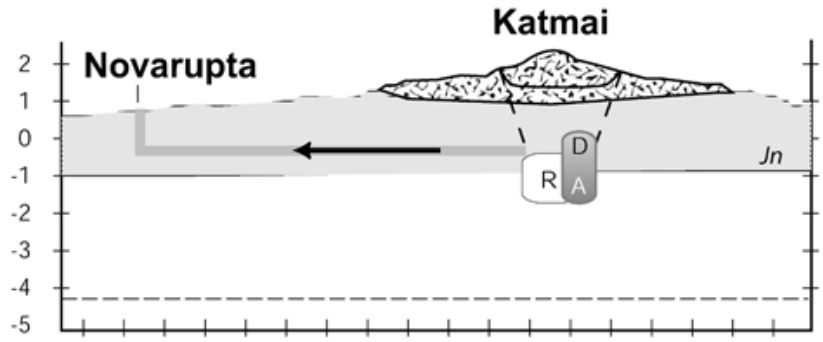

b. All magmas H_2O-saturated, separate storage

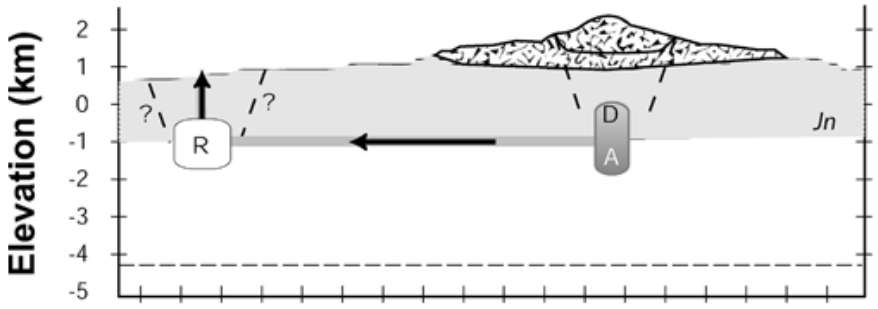

c. Variable H_2O content andesite and dacite both moderately undersaturated

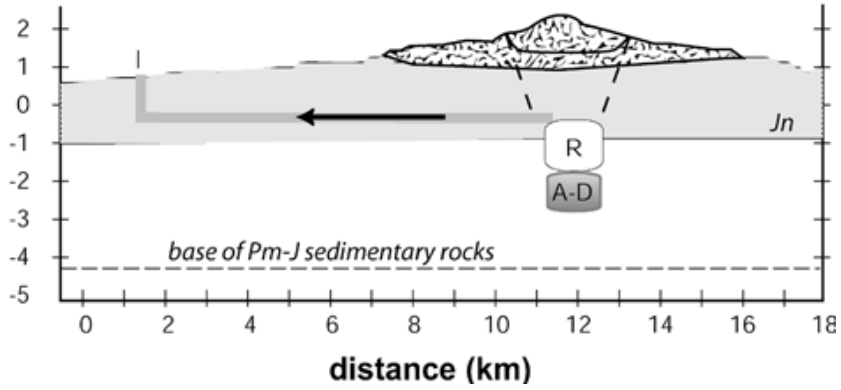

Figure 6. Modified models of magma storages prior to eruption of 1912 (Coombs and Gardners, 2001): a. rhyolitic magma is stored next to andesitic-dacitic magma under Mt. Katmai at water-saturation; b. rhyolitic magma stores under Novarupta and andesitic-dacitic magma stores under Mt. Katmai at water-saturation; c. rhyolitic magma is above the andesitic-dacitic magma at water-undersaturation. R= rhyolite, D= dacite, and A= andesite (Hammer et al., 2002, p. 160).

magma. The composition of the dacitic magma is identical to that of the 1846 eruption (Hildreth & Drake, 1992).

The great eruption of 1932 started and ended with olivine-bearing black andesitic scoria. The initial scoria contained abundant lithics (mostly 1867-47 lavas), 57-62 wt% of SiO_2, and bread crusted dacite blocks at the base. Banding increases toward the top of the flow, and lithics concentration decreases (Hildreth & Drake, 1992). This layer is overlapped by dacitic plinian ash-fall (67-68 wt% SiO_2) with ~16% phenocrysts of plagioclase, hornblende, and hypersthene. It is considered to be >95% of the total 1932 eruption. Coinciding with the dacitic plinian pumice, <0.5% rhyodacite pumice (69-70% SiO_2) was found all over the dacite layer section. It is distinguished by the density difference between rhyodacite (0.26-0.30 g/cm^3) and diorite (0.53-0.78 g/cm^3; Hildreth & Drake, 1992).

Hildreth & Drake (1992) described two pyroclastic flows that occurred at the intraplinian and at the end of plinian phases. The intraplinian ashflow was 0.3-2 m thick with small dacitic ignimbrites rich in lithics fragments and pumice that only extended out to ~2 m from the crater. The late plinian ash-flow reached to Quebrada Azul. The latter deposit was similar to the intraplinian, but contained coarse dacite pumice. The final black scoria settled down onto the ash-flow, marking the terminal event.

Eruption Condition

Electron microprobe analyses of phenocrysts were done by Hildreth and Drake (1992) on deposits from the 1846-47 and 1932 dacitic eruptions. Both eruptions contained similar phenocryst abundances (15-19%), but titanomagnetite was more

abundant in the 1932 dacite, and clinopyroxene was more abundant in 1846-47 dacite. The rhyodacite contained ~50% fewer phenocrysts compared to the dacite. However, it contained more clinopyroxene and less quartz and sanidine. The range of zoning in plagioclase is An_{25-50} for both dacitic deposits and An_{23-39} for the 1932 rhyodacite. There is normal and reverse zoning in all dacite samples, but greater incidence of reverse zoning for those 1846-47. Augite crystals are unzoned and identical at En_{44} Fs_{13} Wo_{43}. Hypersthene crystals range from $En_{69.5-64}$ and $En_{69.5-63}$ for 1946-47 and 1932, respectively. Both augite and hypersthene have a very low CaO ($Wo_{2.0-2.6}$) and modest Al_2O_3 (range 0.4-0.7). Amphiboles are calcic (CaO 10.3-11.9% and 0.5-0.8% K_2O) and

Figure 7. Topographic map of Quizapu, Chile (Hildreth & Drake, 1992, p. 95)

unzoned (Hildreth & Drake, 1992). This implies that dacitic magmas from both eruptions contain at least a few wt% H_2O (Merzbacher & Eggler, 1984).

Crystallization temperature was estimated from Fe-Ti oxide thermometry using ilmenite and titanomagnetite in the dacites and rhyodacite (Figure 8). Estimated temperatures are 837-874°C for the 1846-47 dacite and 863-870°C for the six 1932 dacites. The $\log fO_2$ is within the range of -12.5 and -12 for 1846-47 dacite, and between -12 and -11.5 for the 1932 dacite. For the 1932 dacite, two samples of rhyodacite gave 860°C & 865°C and -11.8 & -11.7 $\log fO_2$, respectively. "This suggests that the minor, phenocrysts-poorer rhyodacite component of the 1932 magma had been situated in a contiguous, thermally equilibrated but possibly water-richer, zone or apophysis of the dacitic reservoir" (Hildreth & Drake,1992, p. 116). The rhyodacite magma might not located near the dacitic magma, because it coincided with the late plinian pumice rather than with early phases of 1932 the eruption (Hildreth & Drake, 1992).

Rutherford found that, for Mt. St. Helens dacites (71-72 wt% SiO_2) at temperatures of 860-870°C, hornblende required a minimum of 125 MPa (>4 km) in H_2O-saturated melt (~4.5 wt.%) to be stable in the melt (Hildreth & Drake, 1992). Hamilton et al. (1964) showed that 4.6% total volatiles require minimum pressure of 120 MPa if the magma is H_2O-saturated, and higher pressure when H_2O-undersaturated (Rutherford, 1985). At depths shallower than 4 km, amphibole should be destabilized. The F content (0.28-0.50 wt%) in Quizapu hornblende could stabilize amphibole at shallower depth, but this effect is unlikely to be large (Hildreth & Drake, 1992).

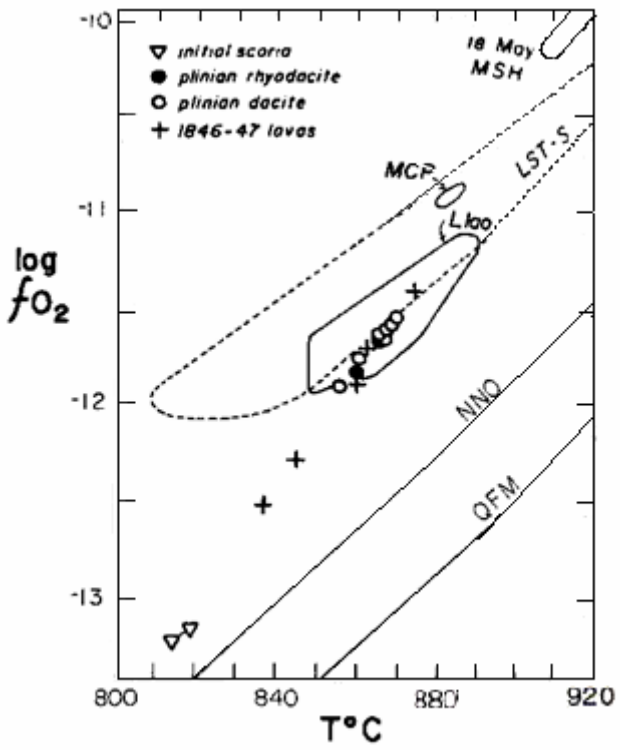

Figure 8. Temperature and oxygen fugacity by Fe-Ti oxide barometry in 1846-47 lavas and 1932 ejecta in Chile (Hildreth & Drake, 1992, p. 118).

Mount St. Helens (MSH), Washington

History of the Eruption

Mount St. Helens (MSH) is considered to have been the most active volcano in the Cascades and Western USA over the past 40,000 years (Mullineaux et al., 1975; Crandell et al., 1975). Pallister et al. (1991) and Gardner et al. (1995) traced eruptions over the past 500 and 4000 years, respectively, and documented aspects of magma evolution that led to recent (1980's) eruptions. Pallister et al. (1991) used past events to present a case for the possibility of predicting future eruptions as MSH. Figure 9 is the satellite image of MSH and nearby features.

The most recent large explosive eruptive event at MSH occurred in May, 1980. The triggering eruptive event occurred on May 18, 1980 at 8:32 A.M. PDT, initiated by an earthquake with a Richter scale magnitude of ~5. Several studies of the eruption ensued (Rutherford et al., 1985; Rutherford and Devine, 1988; Pallister et al., 1991; Cashman, 1992; Rutherford and Hill, 1993; Gardner et al.,1995; Cashman,1988,1992, and Blundy and Cashman (2001, 2005). The May 18 event produced two types of deposits: blast dacite and plinian dacite. The eruption lasted 9 hours. Blast dacite originated from the cryptodome, which formed around late March 1980 (Cashman, 1988). An earthquake caused the collapse of the north flank, exposing the cryptodome at 250 m below the surface (Donnadieu and Merle, 2001), initiating the lateral explosion of the cryptodome. The blast juvenile dacite subdivided into a black dense component (ρ ~ 2300 kg/m^3) and a lower dense gray component (ρ ~ 1600 kg/m^3) (Hoblitt & Harmon, 1993; Cashman & Hoblitt, 2004). The blast dacite was more crystalline (mostly <10 µm) and <0.6 wt % H_2O than the plinian dacite and consisted of microlites (<0.01mm) and microphenocrysts (<0.1 mm) in groundmass and amphibole reaction rims. These characteristics indicated that the cryptodome had degassed substantially and decompressed as magma ascended to a shallower depth or was stored at shallow depth (<5 km) before eruption (Rutherford & Hill, 1993; Cashman, 1988 and 1992; Blundy & Cashman, 2001 and 2005).

The plinian eruption occurred after the explosion of the cryptodome, releasing dacite (white pumice) with ~40% phenocryts (0.5-2 mm) of plagioclase (~An_{48-57}), orthopyroxene, amphibole, Fe-Ti oxides, and rare clinopyroxene (Rutherford et al., 1985). The May 18 dacite did not display any signs of amphibole reaction rims.

Rutherford and Hill (1993) suggested that the absence of amphibole reaction rims and microlites indicated that the magma spent less than 5 days in the ascent from >7 km to the surface.

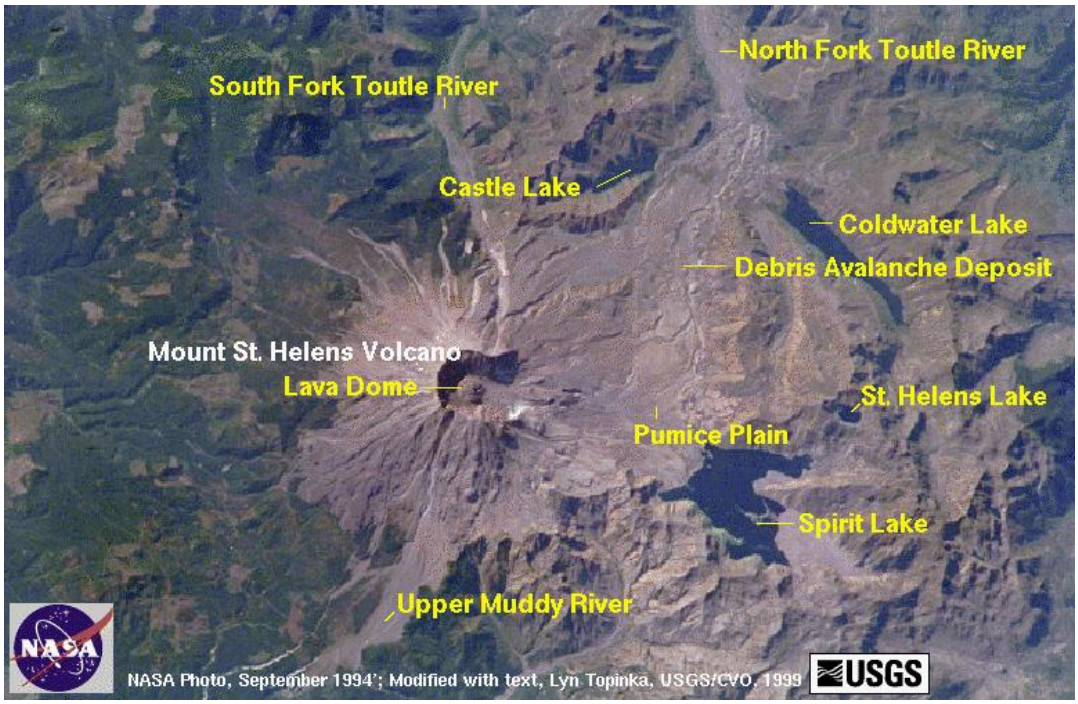

Figure 9. NASA satellite image of Mount St. Helens in 1994. Later added details by Lyn Topinka (Wikipedia website. http://en.wikipedia.org/wiki/Mount_St._Helens)

Eruption Conditions

Rutherford and Devine (1988) determined temperature and pressure conditions and water concentrations of 920°C, 220 MPa >7 km. Depth depths vary from different authors. The magma contained at least X_{H2O} = 0.67 and was water-undersaturated. These conditions marked the low-end amphibole stability field prior to the eruption on May 18 of dacite. These conditions produced phase equilibria close to the natural phenocrysts and glass assemblages (Rutherford et al., 1985). Rutherford and Hill (1993) found that amphibole breakdown started after the magma ascended from depths >7 km, resulting in the pressure dropping below 160 MPa (about 6.5 km depth) at a constant temperature of

900°C. At this point, water-saturation was achieved. Amphibole reaction rims grew as a result of H_2O loss from the coexisting melt during magma ascent along an isotherm, but they also form if the magma is stored in a shallow chamber (<160 MPa) where conditions are outside of the amphibole stability field.

The best estimated temperature ranged from 920-940°C, and $\log fO_2$ ranged from -10.1 to -10.3 (about NNO +1 to 1.5) (Figure 10) that originated from an 8 km magma reservoir with $X_{H2O} = 0.67$. Rutherford et al. (1985) also measured ~4.6 wt% dissolved volatiles (mainly H_2O) in plagioclase melt inclusions, and Rutherford and Devine (1988) found higher dissolved volatiles of ~5 wt% in amphibole inclusions with less SiO_2 (68 wt%) than the plagioclase SiO_2 (73.3 wt%). Their interpretations were based on the following observation:

> "As the bulk SiO_2 content of the melt in the May 18 magma chamber evolved from 68 to 72 wt% SiO_2, the X_{H2O} in the melt was high enough to promote amphibole crystallization and trapping of melt samples with 5.0 wt% volatiles. As long as X_{H2O} was increasing, plagioclase crystallization tended to be suppressed. Then, just prior to the eruption, the X_{H2O} in the melt apparently decreased, causing the surge in plagioclase crystallization (lower An content at rim formed) and entrapment of melt equivalent to the matrix glass but with 4.6 wt% dissolved volatiles (Rutherford & Devine, 1988 p. 11,957)"

The An content of plagioclase that was synthesized experimentally increased with increasing P_{H2O} (or increasing X_{H2O}) on a near-isothermal and near-isobaric basis, which mimiced natural plagioclase An-contents from core- (~An_{57}) to rim- (~An_{50}) forming conditions (Rutherford et al., 1985; Rutherford & Devine, 1988). The An content variation in plagioclase reflected the variation of coexisting liquid composition at 900-920°C and 180-240 MPa (e.g. 75 wt% SiO_2 for the $P_{H2O}/P_{fluid} = X_{H2O} = 0.15$ melt to 66 wt% SiO_2 for the melt crystallizing at $P_{H2O} = P_{fluid} = 220$ MPa => $P_{H2O}/P_{fluid} = X_{H2O} = 1$) on an anhydrous basis (Rutherford et al., 1985). The appearance of amphiboles (i.e. the

low end amphibole field is reached at this point) that are associated with plagioclase produced a plagioclase rim of An_{49} at $X_{H2O} = 0.67$ during isobaric cooling of the magma (Rutherford & Devine, 1988).

Work by Blundy and Cashman (2001) projected the MSH dacite to a Qz-Ab-Or-H_2O system, leading to another explanation of the textural and compositional relationships. They suggested that decompressional fractionation (polybaric), rather than isobaric cooling under water-undersaturated conditions, which Rutherford et al. (1985) and Rutherford and Devine (1988) suggested, is responsible for the magmatic succession. In the water-undersaturated (~4.8 wt%) experiment, plagioclase phenocrysts tended to be resorbed back into the melt until the melt reached water-saturation at 160 MPa under isothermal decompression. However, these conditions produced both lower SiO_2 (less evolved) melt than the natural melt (Rutherford et al. 1985) and variations in wt % of oxides (Rutherford & Devine, 1988). Blundy and Cashman (2001) recalculated the water concentration at 900°C at 220 MPa, by using the model of Moore et al. (1995) and found 5.8±0.4 wt% and 5.5±0.3 wt% at 200 MPa (i.e. very close to water-saturated at 220 MPa and 920°C calculated by the data of Rutherford et al. (1985)), and the phase proportions calculations by using Rutherford et al. (1985). From that, they suggested that amphibole and possibly orthopyroxene, crystallized from ~300 MPa and water-undersaturated conditions to ~200 MPa, where the melt reached water saturation with the appearance of plagioclase (An_{60}) and Fe-Ti oxides. This process is essentially adiabatic, with only a few degrees of temperature drop over ~3 km ascent. As the magma continued to ascend, amphibole was resorbed back into the melt and proportionally decreased, but plagioclase (lower An-content), orthopyroxene, and SiO_2 increased in concentration. By ~150 MPa,

the water content dropped from ~6 wt% to 4 wt% (preserved in melt inclusions in plagioclase crystals), and the melt left the amphibole stability field (Blundy & Cashman, 2001 p. 648 & 2005). Amphibole reaction rims resulted from decompression crystallization and decreased H_2O in the melt concurrently, until syneruptive degassing took over during the eruption (Rutherford & Hill, 1993; Blundy & Cashman, 2005).

The 1980-1986 post-eruptive sequences that were deposited after May 18 were products of magma stored at a shallower depth, at <150 MPa. These eruptions mainly formed lava domes with a range of 62-64.5 wt% SiO_2 (Cashman, 1992; Blundy & Cashman, 2001). The abundant plagioclase phenocrysts in these deposits have well-developed euhedral rims of An_{45-50} and subeuhedral cores of An_{50-60} and An_{80}, where the higher An-contents originated from xenocrysts. Core compositions of plagioclase microphenocrysts ranged from An_{40-48}, similar to the phenocryst rims (Cashman, 1992). The increases of grain size, abundance, and zoning complexities in plagioclase suggested that cooling took place in the shallow magma reservoir under lower temperatures, consistent with lower An-contents (Cashman, 1992), and all supported by Rutherford and Hill's (1993) Fe-Ti oxide barometry. Rutherford and Hill (1993) recorded a temperature of 900±20°C and $\log fO_2$ ranged from -11.1 to 11.3 until 1985, which dropped to 860°C in the 1986 eruptions (i.e. overall a slow gradient decrease in temperature from 1980-1985). The decrease in An-content from ~An_{45} to ~An_{32} (from 1980-1986) in the microphenocryst rims is correlated with the decrease in H_2O content mentioned by Rutherford & Devine (1988). Both imply that decompression to shallow depth and degassing of post May 18 eruptions reduced the intensity from explosive to dome forming lava (Cashman, 1992).

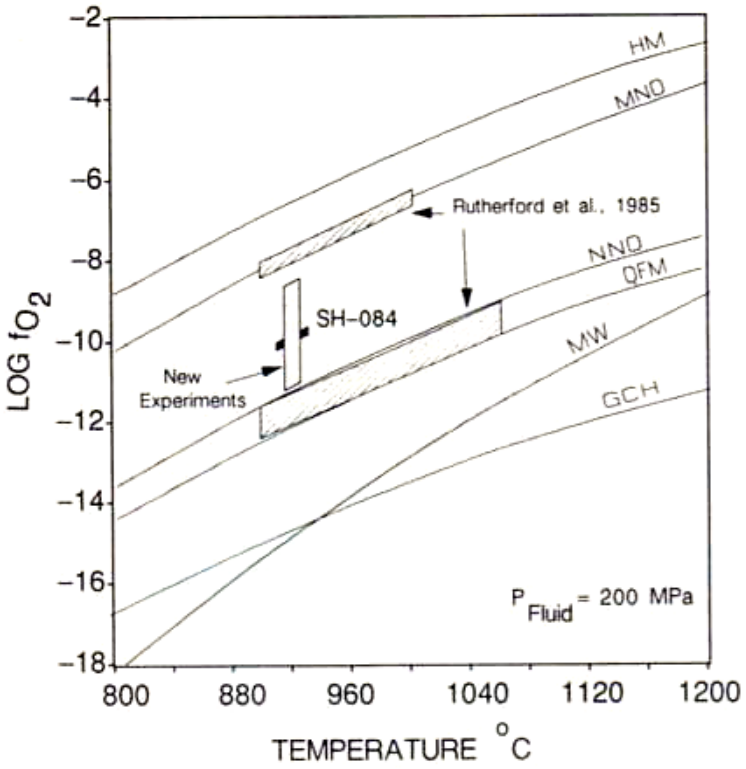

Figure 10. Temperature and oxygen fugacity by Fe-Ti oxide barometry from Mount St. Helens 1980 eruption at fluid pressure = 200 MPa for (Rutherford and Devine, 1988, p. 11,950).

CHAPTER II

ANALYTICAL TECHNIQUES

Methods

micro-XANES Analysis

Descriptions of micro-XANES (or Fe-XANES) measurements have been written by Cartwright (2001 pp. 39-49) and Dyar et al. (2002a pp.516-517). Micro X-Ray Absorption Near Edge Structure spectrometry (micro-XANES) analyses were done at the National Synchrotron Light Source at Brookhaven national Laboratory, New York. The structure of the Fe Kα absorption edge is scanned in the near edge region. Incident beam energies from 50 eV below the main absorption edge energy (7111 eV for Fe) to about 60 eV above the main edge are used. An absorption edge is the mass absorption coefficient (μ_m) of the mineral being studied plotted against the wavelength (a function of wavelength of radiation absorbed and atomic number of an element), and represents the shortest wavelength of incident energy that can cause electrons to be removed from an energy shell of the target atom. The beam is located by the use of an oriented razor blade edge coated with X-ray phosphor, so beam position can be constrained to within <5-15 μm size. The X-ray sampling depth is probably large, but >90% of the signal comes from the top 10μm of the sample. Polished grains of the samples are mounted in the Fe-free epoxy 25 mm lucite disks. A Si(111) channel cut monochromator controls the incident beam energy. The incident X-ray energy is incremented by 0.3 eV intervals over the most critical energy range of -10 to +20 eV relative to the main absorption energy. This provides detailed mapping of the relationship between the pre-edge peak and the main

absorption edge for comparison with the magnetite standard for which the pre-edge position is arbitrarily defined as 0.0 eV. Between -50 and -30 eV and above +30 eV, the X-ray energy is incremented by larger intervals to reduce data collection times. Each energy interval is counted between 5 and 20 live seconds (depending on the intensity of the main edge signal) for a total XANES spectrum acquisition time of about 20-30 minutes. Counting times are adjusted to obtain at least 10^5 counts per energy step at energies above the absorption edge.

The micro-XANES technique uses systematic shifts in the energy of the pre-edge peak of the Fe Kα-absorption edge (the energy of a pre-edge peak is measured) that vary with oxidation state and coordination (bond strength of Fe-O). For consistency, and to correct for drift in the position of the beam, pre-edge peak positions for each spectrum of each unknown mineral are referenced to the pre-edge peak position of a National Museum of Natural History (NMNH) standard magnetite spectrum run before and after it.

Pre-edge peak energies of unknown plagioclase feldspars are referenced to the pre-edge energy of the known Fe^{3+}/Fe_{Total} ratio of magnetite to derive a correct energy scale, such that

$$Position^{unknown} = Position_{measured}{}^{unknown} - Position_{measured}{}^{Magnetite} \quad (26)$$

Standards used were independently characterized by wet chemistry analysis, optical, and EPR spectroscopy by Hofmiester and Rossman (1984), Coombs (1954), Faye (1969), Scala et al. (1978), and Stewart et al. (1996), and among others. Labradorite from Lake Co., Oregon (66.7% Fe^{3+}), fayalite (0% Fe^{3+}), natural magnetite from the National

Museum of Natural History (NMNH) (66.7% Fe^{3+}), acmite (100% Fe^{3+}), and hematite (100% Fe^{3+}) were used as standards.

Overall, there are many factors that contribute to the error found in the use of the micro-XANES technique for feldspar analysis. First, there is the numerical error associated with multiple fits to each pre-edge spectrum. The pre-edge region (or XANES region) is subtracted from the spectra using a Gaussian curve that fits a baseline to the pre-edge peak. Three or more fits are made to every spectrum and averaged together to find the centroid of the peak. Because the feldspar peak is so intense, and therefore extremely easy to fit, the error for this factor has a standard deviation of 0.05 eV.

Second, there is error introduced from subtracting the pre-edge from the main edge of the spectrum. Rigorous fits to the main edge, and the measurement of "true" $\%Fe^{3+}$, is only possible by explicitly identifying the absorption step associated with the ionization potential of the Fe absorption edge and any other resonances on the main-edge in the near-edge region. However, there are no good models for the main-edge peaks. Therefore we use a spline fit when subtracting the pre-edge from the main-edge region. The spline fit goes on the low energy tail of the main-edge structure, and is essentially an empirical fit of the data around the pre-edge. This empirical procedure avoids the errors inherent in choosing specific models for main-edge peak shapes, and probably contributes little error to the pre-edge centroid determinations.

Next, there are errors associated with the shape of the peak used to fit the pre-edge. Peak shape is essential in deconvolutions of the indicated peak and contributions to peak shape. This is why the centroid of the peak is used in this analysis. A Gaussian fit is

used on the pre-edge peak, and therefore peak shape has no effect on the position of the centroid because most of the shape difference is located in the limbs of the pre-edge.

Fourth, there is a long-term calibration drift (~0.5-1 eV) that is attributed to heating of the monochromator crystals by the very intense incident X-ray beam and/or small drifts in the synchrotron source position. For this reason all of the data collected are normalized to a centroid of a magnetite standard as noted above that is run before and after every three spectra are collected. The estimated total error introduced by this factor is 0.5 eV.

Fifth, XANES spectra of iron in feldspars must be affected by count rates because of the small amount of iron found in the crystal structure. For this reason, longer count times (up to 1 hr) are used to more accurately detect the smaller amounts of iron. The increased count times can cause more significant errors introduced by electronic instabilities, resulting in more noise in the spectra. Because the centroid of the pre-edge peak is used in this study, rather than precise shape, the signal to noise problem introduces little error.

Sixth, the possibility of contamination of the feldspar spectrum by fluorescence from adjoining Fe-richer phases must be considered. Grains as far as 200 microns from the focused position can contaminate the spectra. However, because each mineral has a spectral shape specific to the type of mineral it is, this influence can be easily diagnosed by examining the shape of the main-edge of the spectrum. Scattered fluorescence is avoided by putting aluminum apertures over the beam to focus if specifically on the mineral of interest when other Fe-rich phases are in the beam path.

Finally, the errors inherent in the Fe^{3+} content of the standards must be considered. These errors are introduced and vary depending on the type of method used to initially measure the $\%Fe^{3+}$ in the standards. Hofmeister and Rossman (1984) give errors up to ±15% on their integrated peak intensities resulting from the areas of Fe^{2+} and Fe^{3+} Gaussian components. Bajt et al. (1994) also showed that the Fe^{3+}/ Fe_{Total} ratio estimation from Fe-XANES has an error of 10-15% based on the comparison with Mössbauer and wet-chemical measurements. Wilke et al. (2001) stated that the Fe^{3+} contents can be determined with an accuracy of ±10 mol% provided that the site geometry for each redox state is known.

Microprobe Analysis

Microanalysis of plagioclase was done using the Cameca SX50 electron microprobe in the Department of Geosciences at the University of Massachusetts under the supervision of Dr. Michael Jercinovic. This microprobe is equipped with five wavelength-dispersive spectrometers for quantitative analysis and a PGT-IMIX energy dispersive spectrometer for rapid qualitative analysis. Instrument control and implementation of quantitative analyses are done using the Cameca SXrayN50 operating system running in the Solaris environment in a Sun Sparc-20 computer (Cartwright, 2001).

Mössbauer Analysis

Mössbauer measurements were done at Mount Holyoke College under the supervision of Dr. Darby Dyar. Mössbauer spectroscopy is based on the concept of the Mössbauer effect that was discovered by Rudolf Mössbauer (1958). It was based on the emissions of gamma-rays from an exited state of a nucleus in order to decay to the

ground state of the same isotope. As the emitted gamma-ray encounters a solid sample in the ground state, the sample may absorb the gamma-ray in a resonance recapture process, which is raised to the excited state. The energy difference can be measured by matching the energy of the incident gamma-rays to the exact energy level difference. However, this technique is limited to solid samples in order to minimize the recoil after the emission and absorption. Also, Mössbauer spectroscopy is limited to specific types of elements (^{57}Fe, ^{119}Sn, ^{121}Sb and ^{197}Au) that have isotopes with suitable nuclear transitions. Further parameters by which Mössbauer spectra are evaluated (e.g. isomer shift, quadrupole splitting, and linewidth) are discussed by Dyar's (1984).

Results

Table 2 provides the bulk compositions, temperature, pressure, and fO_2 from VTTS, Quizapu, and MHS deposits derived by many researchers. VTTS sample K-45 is dacite from the top of Layer C that was described by Hildreth (1983). Quizapu Q-81 is rhyodacite pumice described by Hildreth and Drake (1992). MSH is rhyolitic pumice that was collected by Dr. Mike Rhodes. The bulk composition is normalized to H_2O-free 100.35 wt%. The temperature and fO_2 are estimated from Fe-Ti oxide barometry (Figure 5, Figure 8, & Figure 10). The 2.52 wt% H_2O was determined by Penfield analysis by Hildreth, (1983). The 0.79 wt% H_2O was determined by T. Fries and Pribble (Hildreth & Drake, 1992). The pressure is determined by using experiments based on reproducing mineral assemblages and mineral stabilities by constraining temperatures, fO_2, and water concentrations (Hammer et al. 2002; Hildreth & Drake, 1992; Blundy & Cashman, 2001).

Table 3 summarizes partition coefficients derived from the Lundgaard & Tegner (2004) formula (25) using from Table 1 and bulk compositions from Table 2. Based on

the % CaO* (% CaO* = %wt CaO/(%wt CaO + %wt Na_2O)), MSH and VTTS are considered to be sub-alkaline silicate melts and Quizapu is an alkaline silicate melt. The partition coefficients of Fe_2O_3 and FeO between plagioclase and silicate melts shown by the shaded yellow blocks will be used in later calculations.

Low- and High- Resolution Fe-XANES

The NSLS 975 session provided high-resolution XANES measurements that were derived using slightly different methods from previous XANES sessions. The difference between "high" and "low" resolutions is that high resolution uses both Si(111) and Si(311) monochromators instead of Si(111) for low resolution. The Si(311) substantially improved spectral resolution from the 1s→3d (pre-edge) transition (Fischer et al., 2007 Abstract). Therefore, high resolution analyses provide more precise measurement of the Fe-K pre-edge centroid positions and intensities of Fe^{2+} and Fe^{3+}, hence providing a more accurate determination of the redox state of iron (Wilke et al., 2001). By examining the binary mixtures between $^{IV}Fe^{2+}$, $^{IV}Fe^{3+}$, $^{VI}Fe^{2+}$, and $^{VI}Fe^{3+}$, the effect of mixing energies on the centroid position and integrated pre-edge intensity can be determined (Figure 11a). "Examination of the pre-edge features of mechanical mixtures of phases containing different proportions of Fe^{2+} and Fe^{3+} suggests that the pre-edge position and intensity for these mixtures can vary quite non-linearly with the average redox state of Fe"(Wilke et al., 2001 p. 714). For a non-linear relationship between the pre-edge centroid position and Fe^{3+}/Fe_{Total} ratio on Figure 11b, the oxidation state and the coordination number of Fe vary simultaneously. This is shown by the relationship between $^{VI}Fe^{2+}/^{IV}Fe^{3+}$ (octahedral/tetrahedral) and $^{IV}Fe^{2+}/^{VI}Fe^{3+}$ (tetrahedral/octahedral). $^{VI}Fe^{2+}/^{VI}Fe^{3+}$ (octahedral/octahedral) and $^{IV}Fe^{2+}/^{IV}Fe^{3+}$ (tetrahedral/tetrahedral) have a linear

	Mount St. Helens	Quizapu Q-81	VTTS K-45
	Pumice	1932 (Rhyodacite Plumice)	Top of Layer C (Dacite)
	wt. %	wt. %	wt. %
SiO_2	64.27	69.85	64.6
TiO_2	0.64	0.44	0.71
Al_2O_3	17.61	15.54	15.65
FeO*	4.77	2.47	5.21
MnO	0.08	0.07	0.12
MgO	2.01	0.65	2.14
CaO	5.03	1.81	4.97
Na_2O	4.48	5.08	4.2
K_2O	1.32	3.59	1.74
P_2O_5	0.14	0.1	0.135
Total	100.35	99.6	83.115
H_2O		0.79	2.52
% CaO*	52.892%	26.270%	54.198%
T (℃)	880-920	860-865	850-880
Ave. T(℃)	900	862.5	865
P (MPa)	220	125	25-50
log(fO_2)	-10.9 to -11.3	-11.8 to -11.7	-10.9 to -11.3

Table 2. Bulk composition, temperature, pressure, and oxygen fugacity for VTTS, Quizapu, and MSH

	D Fe2O3	D FeO	D Fe2O3/D FeO	
VTTS	0.8538	0.0300	28.43474	sub-alkaline
Quizapu	1.5274	0.0350	43.66310	
MSH	0.7700	0.0272	28.28040	
VTTS	1.22967	0.02685	45.79995	alkaline
Quizapu	2.26529	0.03202	70.74720	
MSH	1.13860	0.02500	45.54319	

Table 3. Iron partition coefficient between plagioclase crystal and melt composition (Pl-Liq)

relationship between the centroid position and Fe^{3+}/Fe_{Total} ratio. Therefore, centroid position provides a more accurate estimation to determine the Fe^{3+}/Fe_{Total} ratio of minerals (Figure 11b).

In session 975, the pre-edge spectra were normalized into two categories (one peak and two peak normalizations) by using the PAN software (previously unavailable) at the NSLS X26a beamline. Figure 12a shows the one peak fit of one plagioclase from MSH where the centroid position was modeled by one Gaussian curve. This is a low-resolution measurement (Table 4). Figure 12b shows the same normalized pre-edge peak. However, it was fit with two Gaussian curves that provide two centroid positions (the smaller peak at lower centroid position and larger peak at higher centroid position). The smaller peak centroid position (lower eV) represents the Fe^{2+} concentration, whereas the larger peak centroid position (higher eV) represents the Fe^{3+} concentration (Wilke et al., 2001). The combination of centroids and areas under the curve are used to calculate the average centroid:

Average Centroid = (peak1) + (peak2-peak1)*(1-% area1) = (% area1)*(peak1) + (% area2)*(peak2) (27)

where % area1 = area1/(area1 + area2), which is used to estimate the $\%Fe^{3+}$ value (Table 5). Both of these estimates are derived from the same linear equation based on a set of standards:

($\%Fe^{3+}$ = 54.911 * (Average Centroid) – 390530.292 (28)

(Figure 13). The linear standard equation (28) assumes that Fe^{3+} and Fe^{2+} are both in the tetrahedral site, because Fe^{2+} and Fe^{3+} in plagioclase is predominately in tetrahedral site (Longhi et al. 1976; Sugawara, 2001). Table 6 shows $\%Fe^{3+}$ variance between the high

and low resolution estimations of session NSLS 975. The high resolution calculations reduce the $\%Fe^{3+}$ estimates within the range of 0.09 to 11.43% when comparing to low resolution calculations. By defining the Fe^{2+} centroid position, it has an impact on the $\%Fe^{3+}$ estimation up to ~11.5% in this study.

Plagioclases Fe-XANES

Analyses were taken from cores and rims of most plagioclase crystals from VTTS, Quizapu, and MSH in order to evaluate and compare Fe^{3+} concentration across the crystallization interval. Individual plagioclase cores and rims represent only two fO_2 condition estimates that were associated with the first appearance and latest growth epoch of the crystal. The core measurement is simply an initial record of Fe^{3+}/Fe_{Total} ratio when plagioclase starts to precipitate from the magma. The rim measurement is the final record of Fe^{3+}/Fe_{Total} ratio when the grain stops accumulating due to temperature decrease or change in magma composition. Larger grains may provide more information than smaller grains because in general, under typical cooling conditions they grew on a longer time period. Therefore, additional measurements in between the core and rim were made on one grain in order to understand more of the fO_2 and the magma evolution trend on the NSLS 642 session.

The low resolution $\%Fe^{3+}$ estimates of the cores and rims of individual plagioclase crystals are plotted in Figure 14a derived from Table 4. The Fe^{3+} error bar is assumed to be up ±15% on the low resolution estimates that based on Bajt et al. (1994) comparison with Mössbauer and wet-chemical measurements. Plagioclase crystals from VTTS have the smallest $\%Fe^{3+}$ variations (between ~81.1 and 90.0%). Plagioclase crystals from Quizapu are intermediate and range from ~75.8-93.8%. Plagioclase crystals

Session	Site Location	Sample Name	(Fe3+)/(Fe Total)
642	Katmai K-41	Katmai K-45-1A	0.801
642	Katmai K-41	Katmai K-45-2A	0.897
642	Katmai K-41	Katmai K-45-3A	0.857
642	Katmai K-41	Katmai K-45-4A	0.879
642	Quizapu Q-81	Quizapu Q-81-1-A (center)	0.846
642	Quizapu Q-81	Quizapu Q-81-1-B	0.932
642	Quizapu Q-81	Quizapu Q-81-1-C	0.767
642	Quizapu Q-81	Quizapu Q-81-1-D (rim)	0.843
642	Quizapu Q-81	Quizapu Q-81-5-A	0.916
642	Quizapu Q-81	Quizapu Q-81-2-A	0.868
642	Quizapu Q-81	Quizapu Q-81-6-A	0.899
642	Quizapu Q-81	Quizapu Q-81-4-A	0.909
642	Quizapu Q-81	Quizapu Q-81-8-A	0.797
975	Mount St. Helens	msh1plagcenter.084	0.857
975	Mount St. Helens	msh1plagrim.085	0.832
975	Mount St. Helens	msh2plagcenter.086	0.824
975	Mount St. Helens	msh2plagrim.087	0.826
975	Mount St. Helens	msh3plagcenter.088	0.736
975	Mount St. Helens	msh3plagrim.098	0.854
975	Mount St. Helens	msh5plagcenter.101	0.854
975	Mount St. Helens	msh5plagrim.102	0.848
975	Mount St. Helens	msh6plagcenter.103	0.892
975	Mount St. Helens	msh6plagrim.104	0.991
975	Mount St. Helens	msh7plagcenter.105	0.848
975	Mount St. Helens	msh7plagrim.106	0.826
975	Quizapu Q-81	qui1center.128	0.828
975	Quizapu Q-81	qui1rim.129	0.759
975	Quizapu Q-81	qui2center.130	0.881
975	Quizapu Q-81	qui2rim.131	0.883
975	Quizapu Q-81	qui3center.132	0.868
975	Quizapu Q-81	qui3rim.133	0.903
975	Quizapu Q-81	qui4center.134	0.938
975	Quizapu Q-81	qui4rim.135	0.934
975	Katmai K-41	kat1center.143	0.864
975	Katmai K-41	kat1rim.144	0.885
975	Katmai K-41	kat2center.145	0.813
975	Katmai K-41	kat2rim.146	0.900
975	Katmai K-41	kat3center.147	0.850
975	Katmai K-41	kat3rim.148	0.811

Table 4. Plagioclases' Fe-XANES low resolution measurements

Session	Site Location	Sample Name	(Fe3+)/(Fe Total)
975	Mount St. Helens	msh1plagcenter.084	0.841
975	Mount St. Helens	msh1plagrim.085	0.740
975	Mount St. Helens	msh2plagcenter.086	0.769
975	Mount St. Helens	msh2plagrim.087	0.801
975	Mount St. Helens	msh3plagcenter.088	0.628
975	Mount St. Helens	msh3plagrim.098	0.754
975	Mount St. Helens	msh5plagcenter.101	0.780
975	Mount St. Helens	msh5plagrim.102	0.783
975	Mount St. Helens	msh6plagcenter.103	0.891
975	Mount St. Helens	msh6plagrim.104	0.912
975	Mount St. Helens	msh7plagcenter.105	0.734
975	Mount St. Helens	msh7plagrim.106	0.737
975	Quizapu Q-81	qui1center.128	0.785
975	Quizapu Q-81	qui1rim.129	0.664
975	Quizapu Q-81	qui2center.130	0.799
975	Quizapu Q-81	qui2rim.131	0.814
975	Quizapu Q-81	qui3center.132	0.794
975	Quizapu Q-81	qui3rim.133	0.886
975	Quizapu Q-81	qui4center.134	0.918
975	Quizapu Q-81	qui4rim.135	0.896
975	Katmai K-41	kat1center.143	0.783
975	Katmai K-41	kat1rim.144	0.839
975	Katmai K-41	kat2center.145	0.725
975	Katmai K-41	kat2rim.146	0.872
975	Katmai K-41	kat3center.147	0.811
975	Katmai K-41	kat3rim.148	0.698

Table 5. Plagioclases' Fe-XANES high resolution measurements

Sample Name	Low Resolution	High Resolution	Variance
msh1plagcenter.084	85.7%	84.1%	1.6%
msh1plagrim.085	83.2%	74.0%	9.2%
msh2plagcenter.086	82.4%	76.9%	5.4%
msh2plagrim.087	82.6%	80.1%	2.6%
msh3plagcenter.088	73.6%	62.8%	10.8%
msh3plagrim.098	85.4%	75.4%	10.0%
msh5plagcenter.101	85.4%	78.0%	7.4%
msh5plagrim.102	84.8%	78.3%	6.5%
msh6plagcenter.103	89.2%	89.1%	0.1%
msh6plagrim.104	99.1%	91.2%	8.0%
msh7plagcenter.105	84.8%	73.4%	11.4%
msh7plagrim.106	82.6%	73.7%	8.9%
qui1center.128	82.8%	78.5%	4.3%
qui1rim.129	75.9%	66.4%	9.4%
qui2center.130	88.1%	79.9%	8.3%
qui2rim.131	88.3%	81.4%	7.0%
qui3center.132	86.8%	79.4%	7.5%
qui3rim.133	90.3%	88.6%	1.7%
qui4center.134	93.8%	91.8%	2.0%
qui4rim.135	93.4%	89.6%	3.8%
kat1center.143	86.4%	78.3%	8.1%
kat1rim.144	88.5%	83.9%	4.7%
kat2center.145	81.3%	72.5%	8.8%
kat2rim.146	90.0%	87.2%	2.8%
kat3center.147	85.0%	81.1%	3.9%
kat3rim.148	81.1%	69.8%	11.3%

Table 6. NSLS session 975 Fe-XANES %Fe^{3+} high and low resolutions comparison

a.

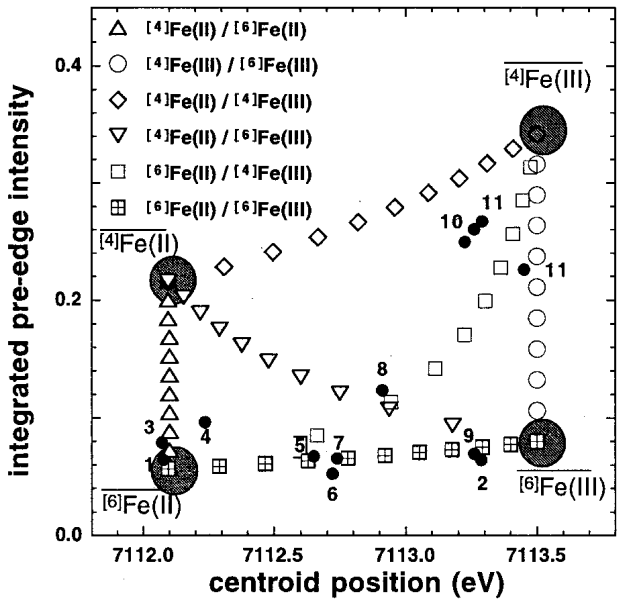

b.

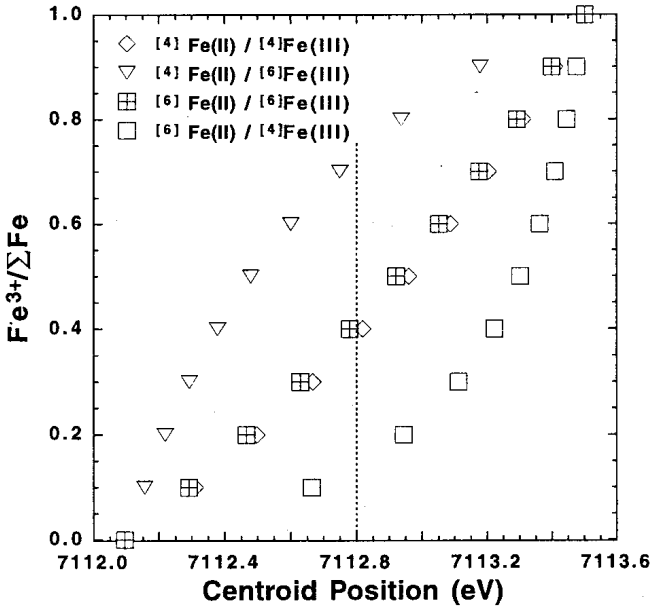

Figure 11. a. The binary mixtures of $^{IV}Fe^{2+}$, $^{IV}Fe^{3+}$, $^{VI}Fe^{2+}$, and $^{VI}Fe^{3+}$ between the centroid position and integrated pre-edge intensity. The black circles are 1 humite; 2 rhodonite no. 1; 3 rhondonite no. 2; 4 dumortierite; 5 potassian kaersutite; 6 kaersutite; 7 vesuvianite no. 1; 8 vesuvianite no. 2; 9 franklinite; 10 magnetite no. 1 & no. 2; 11 labradorite; 12 maghemite. b. The relationship between centroid position and Fe^{3+} percentage (Wilke et al. (2001) p. 724).

a.

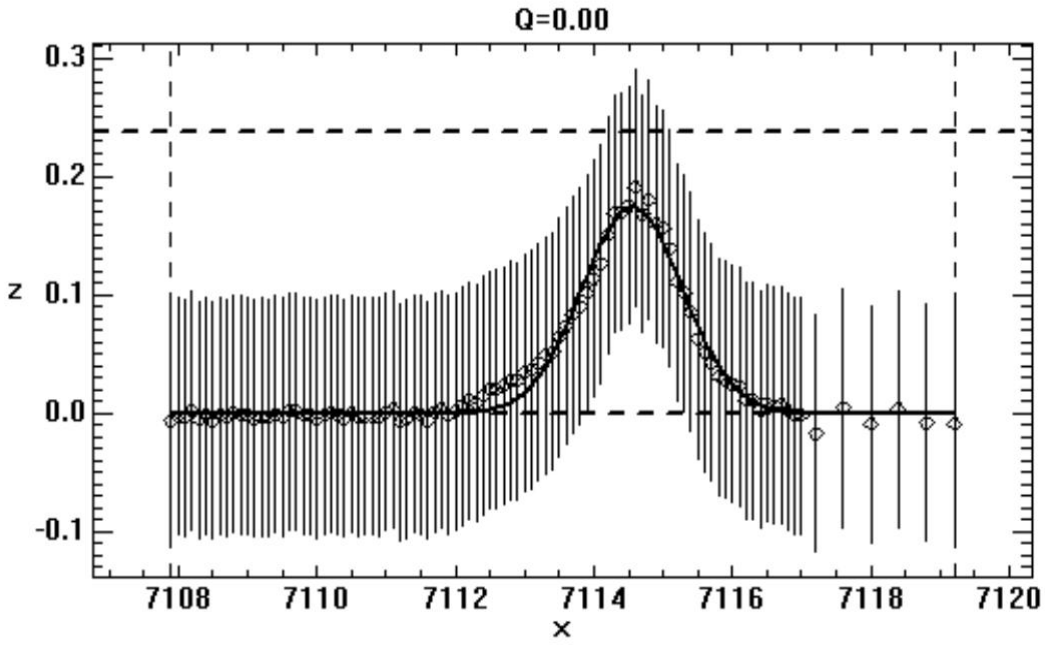

b.

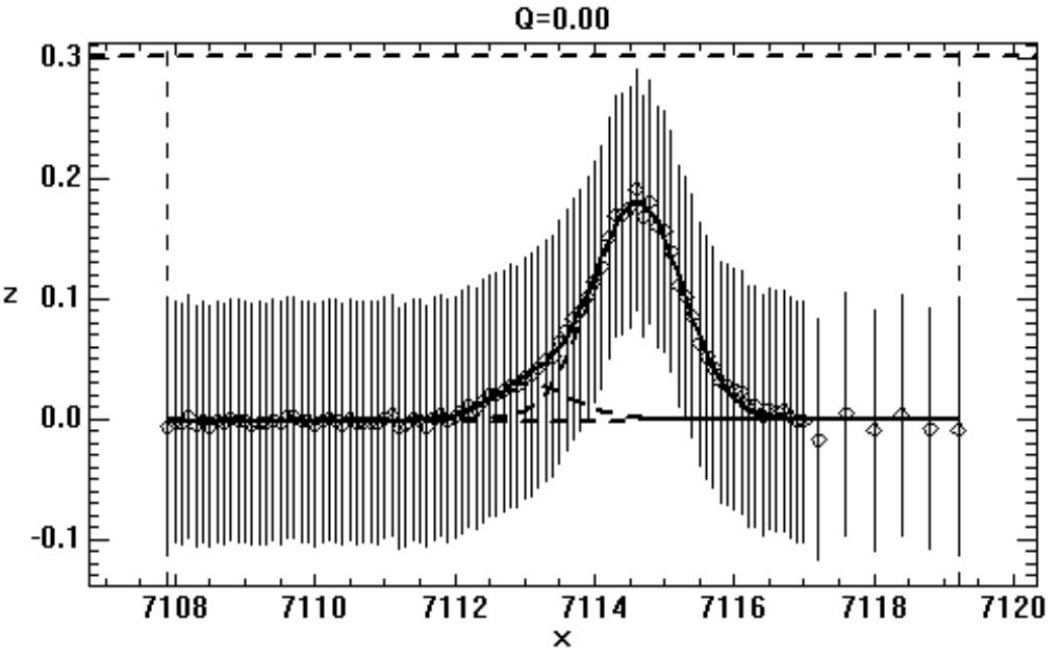

Figure 12. Image of Fe-XANES pre-edge spectra normalization of a plagioclase crystal using the PAN software. This is one of the sample from the Mount St. Helens plagioclase that measured at the NSLS X26a beamline. a. The fit of the pre-edge uses one Gaussian curve (low-resolution). b. The fit uses two Gaussian curves (high-resolution).

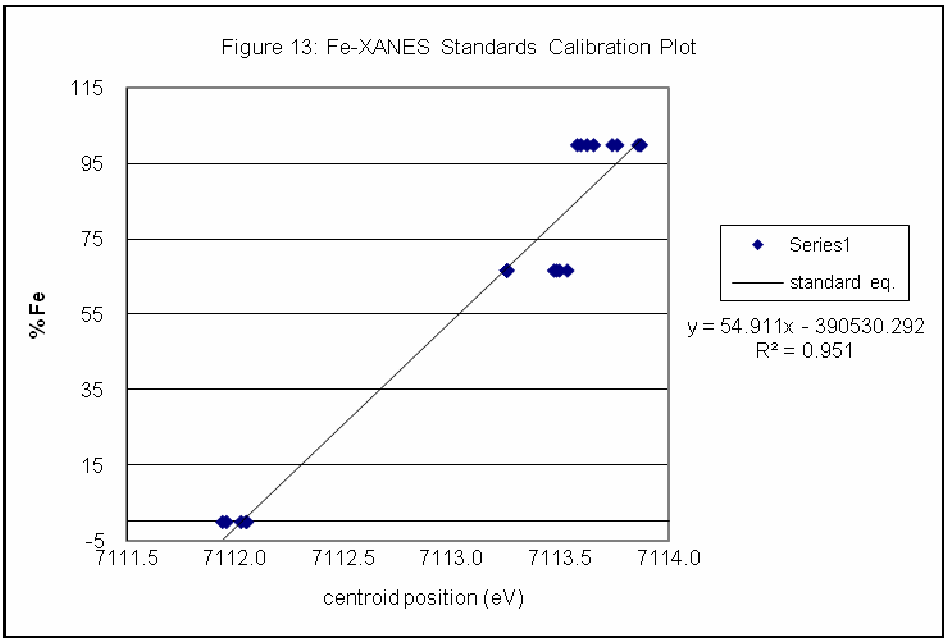

Figure 13. Linear equation derives from the standards from Labradorite from Lake Co., Oregon, fayalite, natural magnetite from the National Museum of Natural History (NMNH), acmite, and hematite. The R^2 is 0.951.

from MSH have the largest range (~73.5-99.1%). The large range of $\%Fe^{3+}$ indicates high fluctuation Fe^{3+}/Fe_{Total} ratio in the magma chamber due to changes in pressure, temperature, fO_2, fH_2O, and magma compositions. The high resolution $\%Fe^{3+}$ is shown on Figure 14b and is derived from Table 5. VTTS, Quizapu, and MSH are range from ~69.8-87.2%, ~66.4-91.8%, and ~62.8-91.2%, respectively. The Fe^{3+} error bar is assumed to be up to ±10% on the high resolution estimates when the Fe^{3+} and Fe^{2+} site geometries are known (Wilke et al., 2001).

Two main observations can be made by comparing the high and low resolution measurements. First, the high resolution range between the core and rim increased from ~8.9% to ~17.4% for Katmai, from ~18% to ~25.4% for Quizapu, and ~25.6% to ~28.4% for MSH. The high resolution measurements were derived from the intensity and the area of two peaks, so they can precisely narrow down the average centroid for more accurate

estimates. Second, high resolution $\%Fe^{3+}$ estimates are ~0.09 to 11.43% lower than the low resolution measurements (Table 6). The decrease of Fe^{3+} content is caused by the precise location of the Fe^{2+} position, which shifts the average centroid towards the lower energy level.

Low Resolution Fe-XANES: VTTS

Plagioclase crystals from VTTS sample K-45 have an estimated $\%Fe^{3+}$ range that is the smallest of the three sites studied. Fe^{3+} spans a range of 80% to 90% based on analyses of seven plagioclase crystals (Figure 15a). Two out of three core and rim measurements during the NSLS 795 session showed iron content evolving to higher Fe^{3+} content from core to rim. The $\%Fe^{3+}$ of one plagioclase crystal dropped ~4% from 85% to 81% from core to rim, which might not be significant enough to determine The 81% rim is relatively close to two plagioclase crystals with center Fe^{3+}/Fe_{Total} ratio values of 80% from NSLS 642 and 81.3% from NSLS 975. It may represent the $\%Fe^{3+}$ stabile in the early magma conditions and increases to 90% prior to the eruption appeared on the Figure 15a.

Low Resolution Fe-XANES: Quizapu

A total of ten plagioclase crystals from thin section Q-81 site were measured: four plagioclases centers and rims, five centers, and one 4-point traverse (Figure 15b). The 4-point measurement of plagioclase provides a map of the general path of Quizapu magma condition changes, and is within the 20% Fe^{3+} range. Other nine plagioclase crystals have Fe^{3+}/Fe_{Total} ratio that would fit in along the path. Four plagioclase cores and rims vary greatly; one increases in $\%Fe^{3+}$ from 86 to 90%, one decreases in $\%Fe^{3+}$ from 82 to 75.8%, and two are relatively stable at 88% and 93.5%. Five core measurements were

91.57%, 86.77%, 89.88%, 90.95%, and 79.72%, which are within the Fe^{3+} percentage range.

The path indicates an increase of Fe^{3+} content up to 94% early in the growth history of plagioclase crystals. Than the Fe^{3+} content dropped to 73%. Finally it rose back up to 84%. Hildreth and Brake (1992) microprobe analyses on plagioclases crystals showed that normal and reverse zoning coexist in1846-47 and 1932 dacite samples. Therefore, the change in plagioclase An content effects the Fe^{3+} content into its crystal structure (Hofmeister & Rossman, 1984). The high Fe^{3+} content could be caused by the

Session	Sample Name	SiO2	Al2O3	CaO	FeO*	Na2O	K2O	Total
975	msh1plagcenter.084	57.633	26.921	8.935	0.279	4.945	0.173	98.886
975	msh1plagrim.085	55.610	27.829	10.161	0.336	4.683	0.128	98.748
975	msh2plagcenter.086	53.700	28.664	11.068	0.182	4.199	0.114	97.925
975	msh2plagrim.087	56.200	27.876	9.905	0.357	4.500	0.143	98.980
975	msh3plagcenter.088	53.423	29.855	12.245	0.264	3.543	0.098	99.428
975	msh3plagrim.098	55.066	28.478	10.476	0.306	4.241	0.135	98.702
975	msh5plagcenter.101	54.000	29.310	11.208	0.231	4.016	0.100	98.865
975	msh5plagrim.102	56.911	27.670	9.631	0.293	4.838	0.147	99.489
975	msh6plagcenter.103	54.575	28.265	10.516	0.318	4.276	0.128	98.079
975	msh6plagrim.104	54.025	29.279	11.491	0.306	3.900	0.108	99.109
975	msh7plagcenter.105	54.664	28.452	10.726	0.297	4.316	0.113	98.568
975	msh7plagrim.106	55.081	27.900	10.346	0.273	4.520	0.144	98.264
975	qui1center.128	60.127	24.808	6.503	0.270	7.607	0.549	99.863
975	qui1rim.129	60.043	25.251	6.684	0.300	7.709	0.525	100.511
975	qui2center.130	59.733	24.394	6.409	0.364	7.795	0.608	99.303
975	qui2rim.131	61.353	24.585	5.775	0.308	7.960	0.630	100.610
975	qui3center.132	59.561	25.270	7.011	0.300	7.475	0.523	100.141
975	qui3rim.133	57.052	26.028	8.383	0.336	6.625	0.464	98.886
975	qui4center.134	61.426	24.564	6.030	0.323	7.836	0.600	100.780
975	qui4rim.135	59.254	24.748	6.617	0.399	7.668	0.558	99.242
975	kat1center.143	56.785	26.339	8.988	0.477	6.454	0.345	99.387
975	kat1rim.144	56.360	25.539	8.366	0.444	7.187	0.330	98.225
975	kat2center.145	59.432	25.548	7.420	0.370	7.190	0.415	100.375
975	kat2rim.146	61.198	25.274	6.960	0.397	7.626	0.366	101.821
975	kat3center.147	55.090	25.292	8.477	0.419	6.390	0.635	96.303
975	kat3rim.148	58.108	24.088	7.133	0.370	7.395	0.379	97.472

Table 7. Microprobe analyses of plagioclase crystal composition

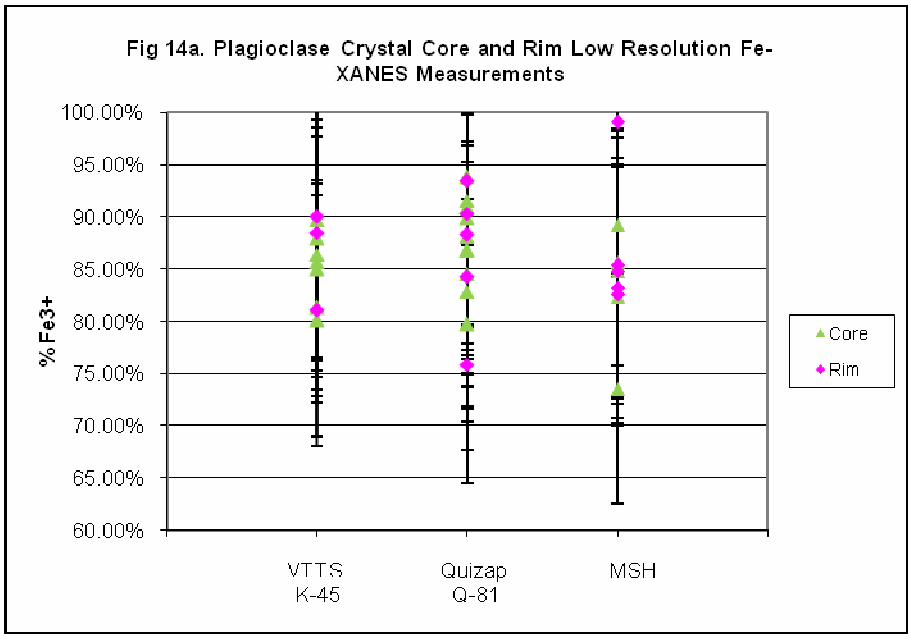

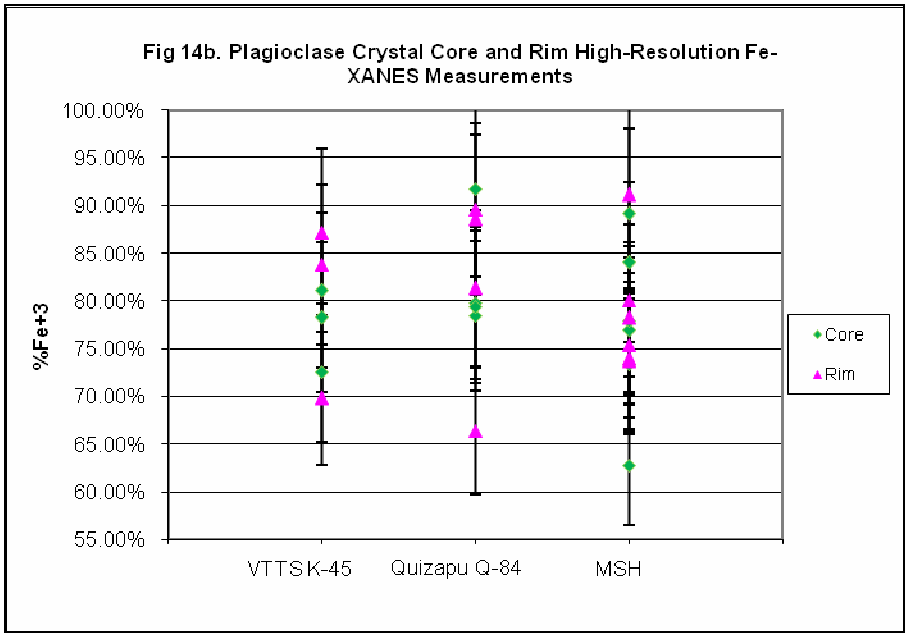

Figure 14. Plagioclase crystal core and rim Fe-XANES measurements: high- and low-resolution. a. Core and rim $\%Fe^{3+}$ measurements in plagioclase crystals core and rim used one peak centroid from sessions NSLS 642 and NSLS 975. The error bar is ±15% (Bajt et al. 1994). b. Core and rim $\%Fe^{3+}$ measurements in plagioclase crystals core and rim used two peak centroids from session NSLS 975. The error bar is ±10% (Wilke et al., 2001).

upward movement of the magma chamber to a more shallow depth (i.e. low pressure enhances fO_2, water saturation, and Fe^{3+}/Fe_{Total} ratio (Rutherford et al., 1985; Popp et al., 1995; and Blundy & Cashman, 2001), decrease in temperature, change in H_2O concentration, and/or influx of another more oxidized source.

Low Resolution Fe-XANES: MSH

MSH plagioclase crystals show considerable diversity in $\%Fe^{3+}$, ranging from ~73-99% Fe^{3+} (Figure 15c). Two out of six plagioclase crystals show around 10% increase of Fe^{3+} from core to rim, and overlapped each other. The rest of them show only approximately 2% variation between core and rim, mostly decreases in $\%Fe^{3+}$. These plagioclase crystals cluster between 83-85% Fe^{3+} content that implies a stable Fe^{3+}/Fe_{Total} ratio condition in the magma chamber during the plagioclase crystals crystallization.

High Resolution Fe-XANES: VTTS, Quizapu, and MSH

Figure 16 provides a high resolution pattern of Fe^{3+}/Fe_{Total} ratio between the rim and core of a plagioclase crystal with ±10% error bar. The shape was very similar to the low resolution pattern. Plagioclase from VTTS (Figure 16a) have 69-88% Fe^{3+}/Fe_{Total} ratio range, which are twice the range comparing to Figure 15a. Quizapu (Figure 16b) plagioclase do not overlap with each other, which makes it difficult interpret the evolution path comparing to Figure 15b. The Fe^{3+}/Fe_{Total} ratio range is 66-92%. MSH (Figure 16c) still shows an increasing pattern of percentage of Fe^{3+} from core to rim. One plagioclase crystal showed a ~10% decline in $\%Fe^{3+}$ in high resolution and ~2.5% declines in low resolution, because of the increased intensity and area of the Fe^{2+} peak.

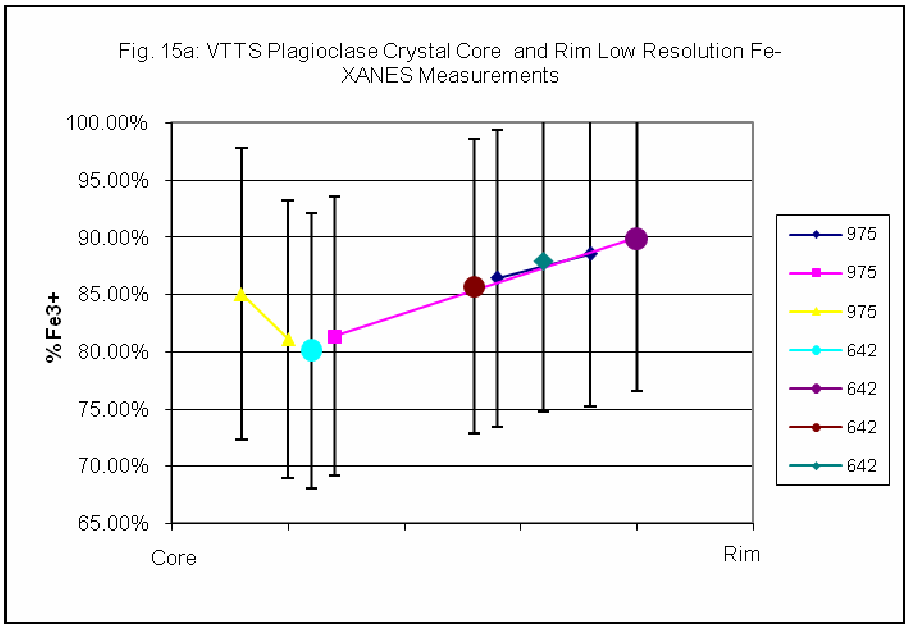
Fig. 15a: VTTS Plagioclase Crystal Core and Rim Low Resolution Fe-XANES Measurements
100.00%
95.00%
90.00%
85.00%
80.00%
75.00%
70.00%
65.00%
%Fe3+
Core
Rim
975
975
975
642
642
642
642

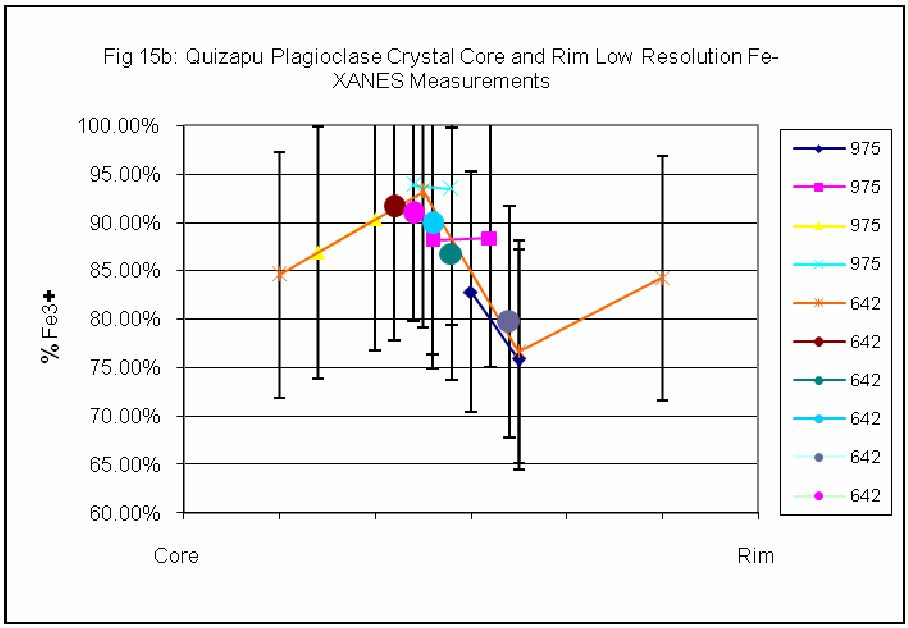
Fig 15b: Quizapu Plagioclase Crystal Core and Rim Low Resolution Fe-XANES Measurements
100.00%
95.00%
90.00%
85.00%
80.00%
75.00%
70.00%
65.00%
60.00%
%Fe3+
Core
Rim
975
975
975
975
642
642
642
642
642
642

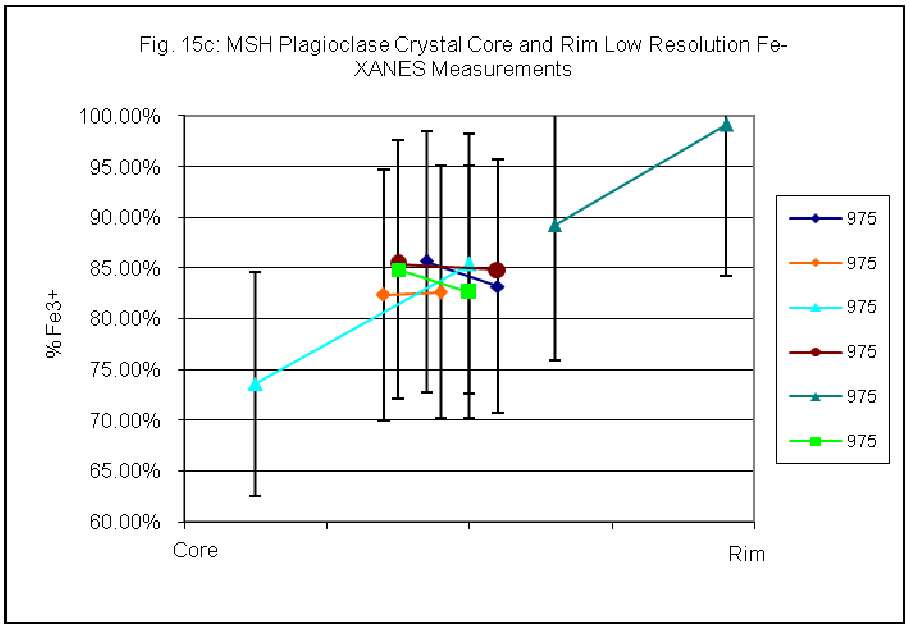

Figure 15. Plagioclase crystal Fe-XANES low resolution measurements from sessions NSLS 642 and 975. Each line represents one plagioclase crystal core-rim measurements where the left point is core and right point is the rim. The error bar is ±15% (Bait et al. 1994). a. Katmai, b. Quizapu, and c. MSH

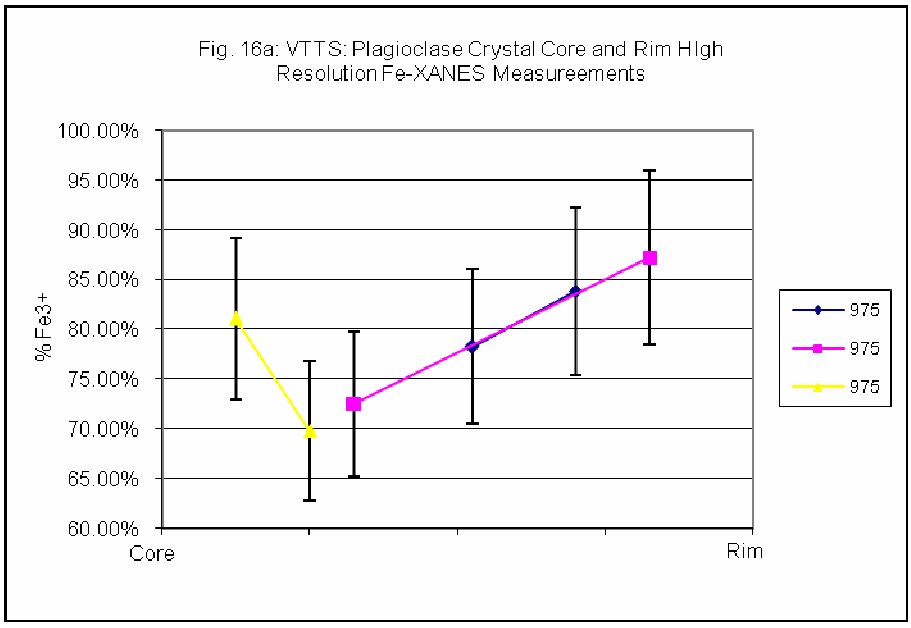

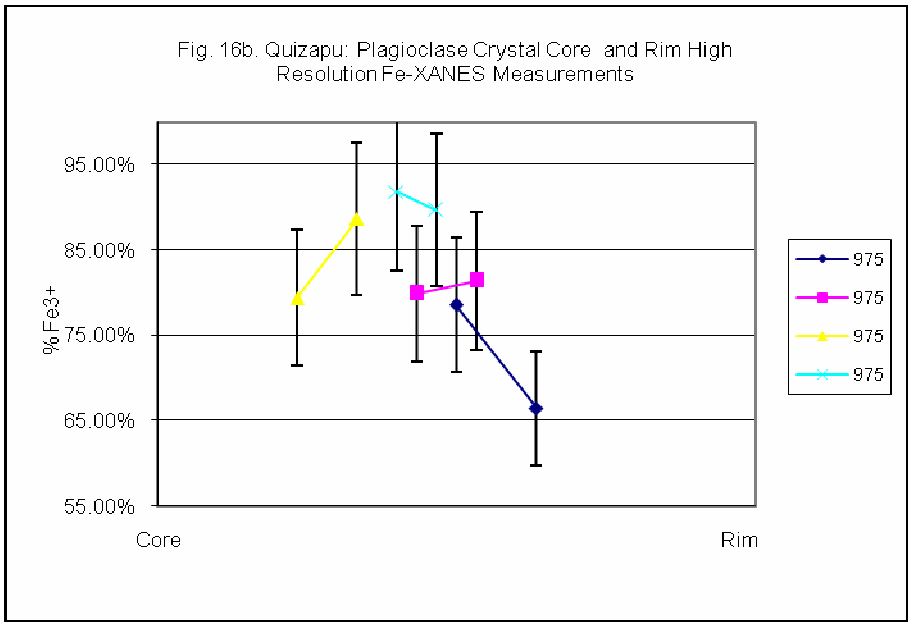

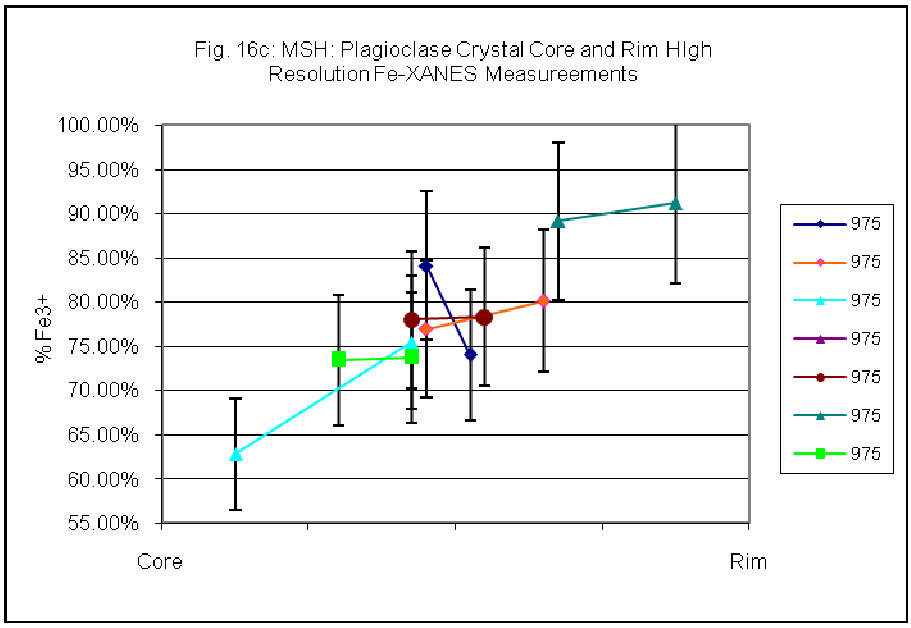

Figure 16. Plagioclase crystal Fe-XANES high resolution measurements from sessions NSLS 975. Fe^{3+} variations are very similar to those shown in Figures 15a-c measurements at low resolution. Each line represents one plagioclase crystal core-rim measurements where the left point is core and right point is the rim. The error bar is ±10% (Wilke et al., 2001). a. Katmai, b. Quizapu, and c. MSH

Microprobe analyses were done on the same spots from which Fe-XANES analyses were collected (Table 7). Microprobe analyses were done to determine the total Fe concentration (FeO*) in the plagioclase crystals. With total Fe concentration determined from the microprobe analyses, iron can be separated into wt% FeO and wt% Fe_2O_3 using $\%Fe^{3+}$ from the high resolution Fe-XANES estimations:

$$\text{wt\% FeO} = [\underline{\text{wt\% FeO}_{\text{microprobe}}} / 1 + (\%Fe^{3+}/(100 - \%Fe^{3+}))] \;\&$$

$$\text{wt\%}Fe_2O_3 = [\underline{\text{wt\% FeO}_{\text{microprobe}} * (\%Fe^{3+}) * (79.86)}/ 71.844]) \qquad (29)$$

Estimates of wt% FeO and wt% Fe_2O_3 of plagioclase crystals are shown in Table 8 with the calculated partition coefficient of plagioclase crystal. The next process is to determine the wt% of Fe_2O_3 and FeO in the melt using equation (24) Lundgaard & Tegner (2004). Tables 3 & 8 were used in the calculations to determine the wt% of Fe_2O_3 and FeO in the melt (Table 10).

Estimated Oxygen Fugacities

In general, fO_2 is more dependent on temperature than on other controlling factors, as shown on Figure 1. Changes in temperature have a direct impact on the $\log fO_2$ value. In this study, temperatures are held constant, so the fO_2 can be determined independently of temperature. Average temperatures of 865°C, 862.5°C, and 900°C is used in the Kress and Carmichael empirical formula for VTTS, Quizapu, and MSH samples, respectively.

Table 10 is the result of the calculation of wt% Fe_2O_3, wt% FeO, and $\log fO_2$ in the melt. The wt% Fe_2O_3, wt% FeO, and $\log fO_2$ of the melt were calculated using Tables 3, 8, and 9. There are two estimated $\log fO_2$ values based on the CAFS and NAFS systems. The CAFS is the best fit parameters for $CaO\text{-}Al_2O_3\text{-}Fe_2O_3\text{-}FeO\text{-}SiO_2$ in melts,

which represent the key oxides in Ca-rich silicate melt. The NAFS is the parameters in Na_2O-Al_2O_3-Fe_2O_3-FeO- SiO_2 in melts, which represent the key oxides in Na-rich silicate melt. The coefficients of these two systems are in Table 9 (Kress & Carmichael, 1991 p. 87). The average of CAFS and NAFS $\log fO_2$ estimates are based on the ratio of CaO and Na_2O wt% (i.e. %CaO*) for Ca-Na intermediate silicate melt (Table 2).

$$\text{Ave } \log(fO_2) = (\text{CaO*})(\text{CAFS}) + (1 - \text{CaO*})(\text{NAFS}) \qquad (30)$$

The averaged $\log fO_2$ is plotted on Figures 17 a, b, & c for VTTS, Quizapu, and MSH. Estimated VTTS is within the range of -9.480 to -7.996 $\log fO_2$. Quizapu is within the range of -7.451 to -5.921 $\log fO_2$. MSH is within the range of -9.636 to -6.865 $\log fO_2$. The average Fe-Ti oxide barometry values are -11.55 for VTTS, -11.75 for Quizapu, and -10.2 for MSH. Figures 17 a-c also includes the average Fe-Ti oxide value and Mössbauer estimations of Fe^{3+}/Fe_{Total} ratio Quizapu and MSH. The estimated $\log fO_2$ are at least two magnitudes, four magnitudes, and one magnitude more oxidized for the VTTS, Quizapu, and MSH Fe-XANES data, respectively.

Table 11 contains the recalculation of the $D_{Fe2O3/FeO}$ and estimated $\log fO_2$ of the melt where ±10% marginal error included to the Fe-XANES high resolution measurements on Table 6. Two negatives $D_{Fe2O3/FeO}$ at +10% represent the $\%Fe^{3+}$ exceeding 100%, which it couldn't calculate the $\log fO_2$. Table 12 is the variance between Tables 10 and 11 $D_{Fe2O3/FeO}$ and estimated $\log fO_2$. The Table 12 $D_{Fe2O3/FeO}$ shows that the increase of 10% Fe^{3+} has a greater variance range of 0.02-4.19 than by decreasing 10% variance range of 0.01-0.23. The estimated $\log fO_2$ variation is range from 0.44-3.49 and 0.38-1.16 for +10% and -10% marginal errors, respectively. One observation on the +10% marginal error shows a distinctive change in $D_{Fe2O3/FeO}$ and $\log fO_2$ variances at the

boundary line %Fe^{3+} ~94%. The 94% Fe^{3+} boundary line might be the point where Fe^{3+}/Fe_{Total} ratio in plagioclase crystal is independent to the fO_2. The $D_{Fe2O3/FeO}$ and estimated logfO_2 variations change from range 0.02-0.23 to 0.40-4.19 and from range 0.44-1.19 to 1.46-3.49, respectively. It's unusual for the estimated logfO_2 to increase over ~1.5 magnitudes by increasing 10% Fe^{3+} in the Fe-XANES measurements.

Plagioclase Mössbauer

Plagioclase crystals were handpicked from Quizapu and MSH samples for Mössbauer %Fe^{3+} measurements (Table 13). The estimated %Fe^{3+} is 38.3 for Quizapu and 25.7 for MSH. Based on the Mössbauer %Fe^{3+} and one of the microprobe plagioclase crystal compositions (qui2rim.131 and msh5plagcenter.101), the Fe^{2+} and Fe^{3+} wt% are determined. The %Fe^{3+} from Mössbauer analysis is much lower than that determined Fe-XANES. Therefore the Mössbauer data produces less oxidized CAFS, NAFS, and average logfO_2 estimates. The logfO_2 values using Mössbauer are closer to Fe-Ti oxide barometry than the values determined by Fe-XANES (Figure 17 b & c).

Session	Sample Name	Wt% FeO	Wt% Fe2O3	D Fe2O3/FeO
975	msh1plagcenter.084	0.04454	0.26095	5.85819
975	msh1plagrim.085	0.08739	0.27657	3.16487

975	msh2plagcenter.086	0.04188	0.15520	3.70574
975	msh2plagrim.087	0.07111	0.31790	4.47071
975	msh3plagcenter.088	0.09820	0.18429	1.87664
975	msh3plagrim.098	0.07541	0.25643	3.40024
975	msh5plagcenter.101	0.05093	0.20028	3.93277
975	msh5plagrim.102	0.06351	0.25465	4.00969
975	msh6plagcenter.103	0.03454	0.31520	9.12523
975	msh6plagrim.104	0.02707	0.31017	11.45879
975	msh7plagcenter.105	0.07905	0.24249	3.06734
975	msh7plagrim.106	0.07182	0.22385	3.11692
975	qui1center.128	0.05799	0.23566	4.06348
975	qui1rim.129	0.10066	0.22136	2.19907
975	qui2center.130	0.07331	0.32313	4.40785
975	qui2rim.131	0.05736	0.27827	4.85086
975	qui3center.132	0.06177	0.26448	4.28182
975	qui3rim.133	0.03822	0.33057	8.65003
975	qui4center.134	0.02655	0.32986	12.42608
975	qui4rim.135	0.04131	0.39705	9.61201
975	kat1center.143	0.10348	0.41486	4.00920
975	kat1rim.144	0.07163	0.41358	5.77368
975	kat2center.145	0.10164	0.29852	2.93708
975	kat2rim.146	0.05072	0.38481	7.58759
975	kat3center.147	0.07912	0.37736	4.76927
975	kat3rim.148	0.11174	0.28729	2.57100

Table 8. High resolution plagioclase crystal iron partition

	CAFS	**NAFS**	**Units**
a	0.207	--	
b	1.298 x 10^4	1.678 x 10^4	K
c	-6.115	-9.266	
dSiO2	-2.368	0.312	
dAl2O3	-1.622	-0.698	
dNa2O	--	2.065	
dCaO	2.073	--	

Table 9. Best fit parameters for Eq. (16) (Kress & Carmichael, 1991 p. 87)

Session	Sample Name	Wt% FeO	Wt% Fe2O3	D Fe2O3/FeO	CAFS	NAFS	Ave log$fO2$
975	msh1plagcenter.084	1.483	0.306	0.206	-11.70	-3.33	-7.76
975	msh1plagrim.085	2.910	0.324	0.111	-13.04	-3.59	-8.59
975	msh2plagcenter.086	1.395	0.182	0.130	-12.66	-3.53	-8.36
975	msh2plagrim.087	2.368	0.372	0.157	-12.30	-3.44	-8.13
975	msh3plagcenter.088	3.270	0.216	0.066	-14.15	-3.82	-9.28
975	msh3plagrim.098	2.511	0.300	0.120	-12.88	-3.56	-8.49
975	msh5plagcenter.101	1.696	0.235	0.138	-12.54	-3.50	-8.28
975	msh5plagrim.102	2.115	0.298	0.141	-12.52	-3.49	-8.27
975	msh6plagcenter.103	1.150	0.369	0.321	-10.76	-3.13	-7.17
975	msh6plagrim.104	0.901	0.363	0.403	-10.28	-3.04	-6.86
975	msh7plagcenter.105	2.633	0.284	0.108	-13.10	-3.61	-8.63
975	msh7plagrim.106	2.392	0.262	0.110	-13.06	-3.60	-8.60
975	qui1center.128	1.811	0.104	0.057	-14.76	-4.10	-6.90
975	qui1rim.129	3.144	0.098	0.031	-16.10	-4.37	-7.45
975	qui2center.130	2.289	0.143	0.062	-14.61	-4.07	-6.84
975	qui2rim.131	1.792	0.123	0.069	-14.39	-4.03	-6.75
975	qui3center.132	1.929	0.117	0.061	-14.66	-4.08	-6.86
975	qui3rim.133	1.194	0.146	0.122	-13.16	-3.78	-6.24
975	qui4center.134	0.829	0.146	0.176	-12.38	-3.62	-5.92
975	qui4rim.135	1.290	0.175	0.136	-12.94	-3.73	-6.15
975	kat1center.143	3.801	0.539	0.142	-13.28	-3.68	-8.88
975	kat1rim.144	2.631	0.537	0.204	-12.48	-3.52	-8.37
975	kat2center.145	3.733	0.388	0.104	-13.93	-3.82	-9.30
975	kat2rim.146	1.863	0.500	0.268	-11.88	-3.40	-8.00
975	kat3center.147	2.906	0.490	0.169	-12.88	-3.61	-8.63
975	kat3rim.148	4.104	0.373	0.091	-14.22	-3.87	-9.48

Table 10. Iron partition coefficient and oxygen fugacity of the melt composition

Session	Sample Name	Fe3+/FeTotal +10% error	Fe3+/FeTotal -10% error	DFe2O3/FeO		logfO2	
				@ +10%	@ -10%	@ +10%	@ -10%
975	msh1plagcenter.084	94.1%	74.1%	0.618	0.112	-7.76	-8.58
975	msh1plagrim.085	84.0%	64.0%	0.205	0.070	-8.59	-9.23
975	msh2plagcenter.086	86.9%	66.9%	0.260	0.079	-8.36	-9.02
975	msh2plagrim.087	90.1%	70.1%	0.355	0.092	-8.13	-8.86
975	msh3plagcenter.088	72.8%	52.8%	0.105	0.044	-9.28	-9.84
975	msh3plagrim.098	85.4%	65.4%	0.228	0.074	-8.49	-9.14
975	msh5plagcenter.101	88.0%	68.0%	0.286	0.083	-8.28	-8.97
975	msh5plagrim.102	88.3%	68.3%	0.295	0.084	-8.27	-8.96
975	msh6plagcenter.103	99.1%	79.1%	4.514	0.148	-7.17	-8.20
975	msh6plagrim.104	101.2%	81.2%	-3.417	0.168	error	-8.03
975	msh7plagcenter.105	83.4%	63.4%	0.196	0.068	-8.63	-9.26
975	msh7plagrim.106	83.7%	63.7%	0.201	0.069	-8.60	-9.23
975	qui1center.128	88.5%	68.5%	0.121	0.034	-6.90	-7.36
975	qui1rim.129	76.4%	56.4%	0.051	0.020	-7.45	-7.83
975	qui2center.130	89.9%	69.9%	0.139	0.036	-6.84	-7.32
975	qui2rim.131	91.4%	71.4%	0.166	0.039	-6.75	-7.25
975	qui3center.132	89.4%	69.4%	0.132	0.036	-6.86	-7.30
975	qui3rim.133	98.6%	78.6%	1.117	0.058	-6.24	-6.90
975	qui4center.134	101.8%	81.8%	-0.894	0.071	error	-6.72
975	qui4rim.135	99.6%	79.6%	4.281	0.061	-6.15	-6.85
975	kat1center.143	88.3%	68.3%	0.296	0.085	-8.88	-9.60
975	kat1rim.144	93.9%	73.9%	0.600	0.111	-8.37	-9.22
975	kat2center.145	82.5%	62.5%	0.186	0.066	-9.30	-9.93
975	kat2rim.146	97.2%	77.2%	1.376	0.133	-8.00	-8.96
975	kat3center.147	91.1%	71.1%	0.402	0.097	-8.63	-9.40
975	kat3rim.148	79.8%	59.8%	0.155	0.059	-9.48	-10.09

Table 11. The recalculated iron partition coefficient and oxygen fugacity of the melt at high resolution Fe^{3+}/Fe_{Total} values ±10% on Table 6

Session	Sample Name	$D_{Fe2O3/FeO}$ Variance		$\log fO_2$ Variance	
		+10% error	-10% error	+10% error	-10% error
975	msh1plagcenter.084	0.41	0.09	1.46	0.82
975	msh1plagrim.085	0.09	0.04	0.82	0.64
975	msh2plagcenter.086	0.13	0.05	0.92	0.67
975	msh2plagrim.087	0.20	0.07	1.09	0.73
975	msh3plagcenter.088	0.04	0.02	0.62	0.56
975	msh3plagrim.098	0.11	0.05	0.87	0.65
975	msh5plagcenter.101	0.15	0.06	0.97	0.69
975	msh5plagrim.102	0.15	0.06	0.99	0.69
975	msh6plagcenter.103	4.19	0.17	3.49	1.03
975	msh6plagrim.104	-3.82	0.23	error	1.16
975	msh7plagcenter.105	0.09	0.04	0.80	0.63
975	msh7plagrim.106	0.09	0.04	0.81	0.63
975	qui1center.128	0.06	0.02	0.66	0.46
975	qui1rim.129	0.02	0.01	0.44	0.38
975	qui2center.130	0.08	0.03	0.71	0.48
975	qui2rim.131	0.10	0.03	0.78	0.50
975	qui3center.132	0.07	0.02	0.69	0.44
975	qui3rim.133	0.99	0.06	1.94	0.66
975	qui4center.134	-1.07	0.11	error	0.80
975	qui4rim.135	4.14	0.07	3.02	0.70
975	kat1center.143	0.15	0.06	1.02	0.72
975	kat1rim.144	0.40	0.09	1.47	0.84
975	kat2center.145	0.08	0.04	0.80	0.64
975	kat2rim.146	1.11	0.14	2.21	0.96
975	kat3center.147	0.23	0.07	1.19	0.77
975	kat3rim.148	0.06	0.03	0.74	0.61

Table 12. Iron partition coefficient and oxygen fugacity variances between Tables 10 and 11

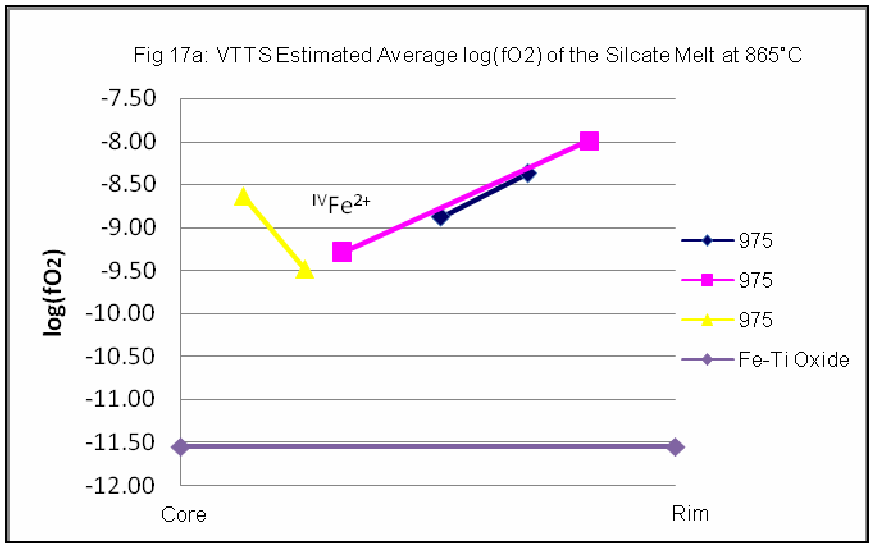

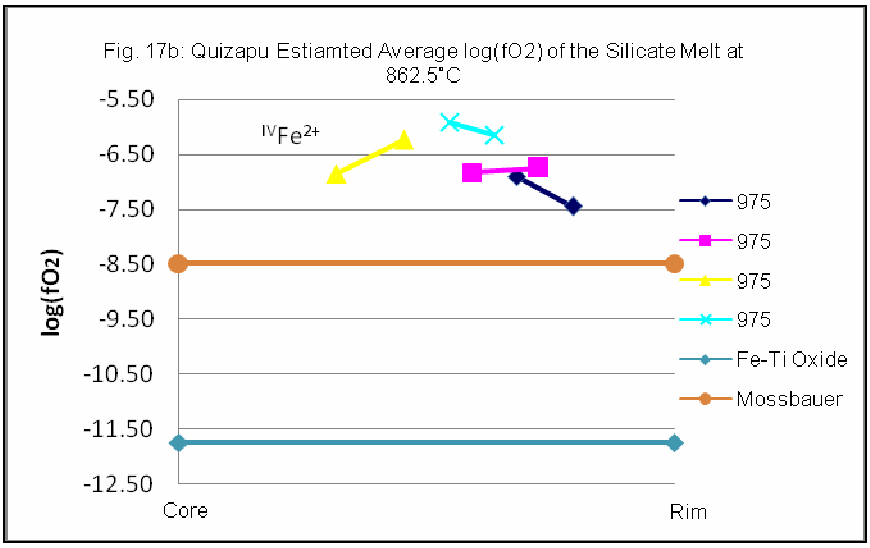

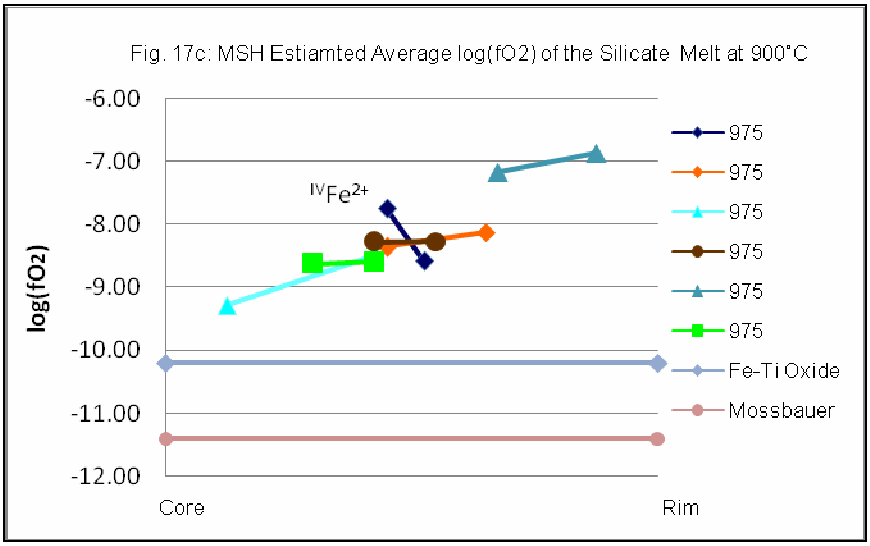

Figure 17. Estimated oxygen fugacity of the silicate melt using high resolution $\%Fe^{3+}$ values. Fe-XANES and Mössbauer estimated $\log fO_2$ calculate from Kress & Carmichael empirical formula. The estimated $\log fO_2$ core-rim pattern is assumed that the Fe^{2+} and Fe^{3+} are in the tetrahedral site. The Fe-Ti oxide barometry value is included. a. VTTS, b. Quizapu, and c. MSH.

		Plagioclase		Silicate Melt		Esitmated logfO_2		
	$\%Fe^{3+}$	Wt% FeO	Wt% Fe_2O_3	Wt% FeO	Wt% Fe_2O_3	CAFS	NAFS	Ave logfO_2
Quizapu qui2rim.131	38.3	0.190	0.131	5.929	0.058	-18.631	-4.869	-8.48
MSH msh5plagcenter.101	25.7	0.172	0.066	5.718	0.077	-17.552	-4.505	-11.41

Table 13. Mössbauer %Fe3+ measurements, iron partition coefficient, and estimated oxygen fugacity

CHAPTER III

FACTORS INFLUENCING OXYGEN FUGACITY

Discussions

Iron is an essential element for evaluating fO_2 during plagioclase crystallization. In this study, plagioclase crystals were used to retrieve the Fe^{3+}/Fe^{2+} ratio through Fe-XANES, microprobe, Mössbauer techniques, leading to an estimate of melt fO_2. The estimated $\log fO_2$ in the melt at a fixed liquidus temperature is show in Table 10. The estimated $\log fO_2$ values are much more oxidized than those based on the Fe-Ti oxide barometry. All Fe-XANES $\log fO_2$ estimates are at least one to four magnitudes more oxidized than those based on Fe-Ti oxide barometry (Figure 17 a-c). Mössbauer $\log fO_2$ estimates of Fe^{3+}/Fe_{Total} ratio are two magnitudes more oxidized in Quizapu and at least one magnitude more reduced in MSH that values based on Fe-Ti oxide barometry. The Fe-XANES and Mössbauer $\log fO_2$ estimates are at least two magnitudes more oxided in Quizapu than in VTTS and MSH, which Quizapu samples produce the most marginal error.

Fe-Ti oxide barometry is based on the composition of Fe-Ti minerals that coexist in the volcanic rock. Plagioclase crystals crystallize and grow in the magma record the Fe^{3+}/Fe^{2+} ratio conditions in the magma chamber over a much longer time than that recorded by Fe-Ti oxide through the crystallization process. Therefore, difference in timing of Fe-Ti oxide growth compared to plagioclase may causes the difference between the fO_2 calculated from Fe-Ti oxide and that calculated based on Fe-XANES measurements.

Kress and Carmichael's empirical formula (1991) applies to Fe-redox equilibrium at one atmosphere for anhydrous silicate melt. However, plagioclase crystals from the three sites crystallized at a higher pressure than one atmosphere and reached water-saturation in the silicate melt prior to eruption. Therefore, the estimated fO_2 does not accurately reflect the plagioclase crystallization conditions in the magma. Water concentration, pressure, and Fe-XANES miscalculation need to be included to the fO_2 estimation. All these factors have the potential to influence the Fe^{3+}/Fe^{2+} ratio in plagioclase crystal and silicate melt.

Effect of %CaO in Plagioclase and Bulk Composition

Three observations possibility associate with the marginal error by %CaO in plagioclase crystal and bulk composition. First, plagioclase An content is lower in Quizapu (An_{23-39}) than in VTTS (An_{34-71}) and MSH (An_{48-57}) (Hildreth & Drake, 1992; Hildreth, 1983; Rutherford et al., 1985). Table 7 microprobe measurements support the An content where most Quizapu sample measurements have higher $\%Na_2O$ than %CaO, vice versa in VTTS and MSH. Second, the Quizapu bulk composition contains ~26.37% CaO*, which was approximately half of the % CaO* on VTTS and MSH bulk compositions. Third, an equation (30) might not base on the ratio of CaO and Na_2O wt% when calculating the average $\log fO_2$ estimates. Further research is needed to identify the percentage of marginal error on the Fe-XANES measurement.

Effect of Water Content

Water content in the magma affects the stability of mineral phases, hydrogen fugacity, fO_2, and Fe^{3+}/Fe^{2+} ratio. The increase of water content causes an increase of Fe^{3+}/Fe^{2+} ratio at a constant fO_2 (Baker & Rutherford, 1996; Botcharnikov et al., 2005).

The measured wt% H_2O of 2.52 for VTTS and 0.79 for Quizapu (Table 3) were measured in bulk compositions of each rock. The wt% H_2O is not measured for MSH sample. Work on the VTTS, Quizapu, and MSH by previous researches shows that there were at least 3 wt% H_2O in these magma prior to their eruptions, and each magma achieved water-saturation as the magma ascending to the surface, based on analyses of melt inclusions and stability of amphibole phenocrysts (Rutherford et al., 1985; Hildreth & Drake, 1992; Rutherford & Hill, 1993, Blundy & Cashman, 2001 & 2005).

Baker & Rutherford (1996) and Gaillard et al. (2001) mentioned that dissolved water in the melt influenced the Fe^{3+}/Fe^{2+} ratio and should be included to the Kress and Carmichael empirical formula for fO_2 < NNO +1. For fO_2 >NNO +1.5, the Fe^{3+}/Fe^{2+} ratio is essentially controlled by the anhydrous melt composition and fO_2 (Gaillard et al., 2001). Based on reaction (16), dissolved hydroxyl content can be added to the empirical formula at a given T, fO_2, and composition. This relationship is defined by:

$$\{X_{Fe2O3}/X_{feO}\} = k * \exp(d_{OH-} * X_{OH-}) \quad (31)$$

where $k = \exp(a\ln fO_2 + b/T + c + \sum d_i X_i)$ (Baker & Rutherford, 1996). It is necessary to determine the hydroxyl concentration in the melt. Based on Fe-Ti oxide barometry, fO_2 from three sites was within NNO +1 to 1.5 suggesting that variation in water concentration had little influence on fO_2 in these cases.

Effect of Pressure

Mo et al. (1982) stated that the Fe_2O_3/FeO ratio decreases with increasing pressure, at constant fO_2 and temperature (Kress and Carmichael, 1991). Kress and Carmichael (1991) expanded their empirical formula by applying it to higher pressure. Their theory is based on the hypothesis from Carmichael and Ghiorso (1986):

> "The equilibrium Fe_2O_3/FeO ratio would decrease to a minimum at the pressure where the change in volume (ΔV) of reaction becomes zero at increasing pressure and fixed fO_2. At pressure higher than this minimum, the equilibrium Fe_2O_3/FeO ratio would increase with pressure. Our results predict that ΔV for the iron-redox reaction remains positive to well over 3 GPa. Therefore, at fixed fO_2, the equilibrium Fe_2O_3/FeO ratio will decrease monotonically with increasing pressure." (Kress and Carmichael, 1991 p. 90)

VTTS, Quizapu, and MSH plagioclase crystals crystallized at 25-50 MPa, 125 MPa, and 220 MPa lesser than 3 GPa, respectively. Therefore, pressure has an inverse relationship with fO_2, as a result of the ΔV of Fe^{3+} in the melt with increased pressure. It might be difficult to distinguish the effect of pressure alone on the Fe^{3+}/Fe_{Total} ratio.

Pressure also has an effect on water activity, which in turn affects Fe^{3+}/Fe^{2+} ratio in the melt. Burnham (1975) and Stolper (1982) showed that mole % H_2O or fH_2O increases nonlinearly with increasing pressure. Burnham (1975) also mentioned that high pressure requires more wt% H_2O to maintain the same aH_2O at a constant temperature. The change in pressure at a constant wt% H_2O can influence aH_2O. For example, Burnham (1974) showed the relationship between aH_2O, wt% H_2O, and pressure. At constant wt% H_2O, the increase of pressure will decrease the aH_2O, which eventually decreases the Fe^{3+}/Fe^{2+} ratio. This supports the results of Botcharnikov et al. (2005). As long as the aH_2O is constant throughout the magmatic process, fO_2 is the main controlling factor of Fe^{3+}/Fe^{2+} ratio in the melt (Figure 2b).

Pressure might be the main influence on the Fe^{3+}/Fe_{Total} ratio in the melt on MSH sample. This supports by Figure 16c where the Fe^{3+}/Fe_{Total} ratio generally increases from core to rim, which agrees with Blundy and Cashman (2001). Blundy and Cashman (2001) showed that the MSH 1980 dacitic magma underwent decompression crystallization and fractionation. The decrease in pressure caused water saturation at pressures ~200 MPa

where plagioclase and orthopyroxene phenocrysts increased in crystallization, and amphibole decreased by being reabsorbed back into the melt during this period (Rutherford and Devine, 1988; Rutherford and Hill, 1996; Blundy and Cashman, 2001). Few plagioclase crystals on Figure 16c show that the Fe^{3+}/Fe_{Total} ratios have ~3% variance between core and rim that might indicate rapid crystal growth in the melt.

Effect of Fe-XANES Measurements

There are seven factors that contribute to error found in the use of the micro-XANES technique for feldspars analysis (summarized on pp. 24-26). Of those seven factors, the last one can be discussed further. The $\%Fe^{3+}$ measurements from the standards are used to calculate the standard linear equation (28), which is used to determine the $\%Fe^{3+}$ in the plagioclase crystals. However, this linear equation might not accurately estimate the $\%Fe^{3+}$ in the plagioclase crystals. Wilke et al. (2001) showed that the pre-edge parameters for labradorite are close to the left of the $^{VI}Fe^{2+}/^{IV}Fe^{3+}$ join. This suggested a partitioning of Fe^{2+} in tetrahedral and octahedral sites (Figure 11a). From Figure 11b, the standard equation should have an exponential curve (square pattern). Therefore, the standard equation should have a nonlinear form rather than the linear form used in this study.

Based on Figure 11b, the variance between $^{IV}Fe^{2+}/^{IV}Fe^{3+}$ (tetrahedral/tetrahedral) and $^{VI}Fe^{2+}/^{IV}Fe^{3+}$ (octahedral/tetrahedral) coordination is between 0 to ~30% Fe^{3+}/Fe_{Total} ratio. The conversion of Fe^{2+} from tetrahedral to octahedral coordination completely needs to reduce 30% Fe^{3+} from the high resolution Fe-XANES measurements on Table 6. Table 14 is the recalculation of the new Fe partition coefficient and averaged $\log fO_2$ after the deduction of 30% from Table 6 high resolution $\%Fe^{3+}$ estimation. The averaged

logfO_2 range between Table 10 and 14 reduces from 1.7-2.3 for VTTS, from 1.1-1.7 for Quizapu, and from 1.7-2.5 for MSH. The recalculated averagedfO_2 archeives a better estimation compared to the Fe-Ti oxide barometry and Mössbauer values (Figure 18). Because the Fe^{2+} in plagioclase can be in octahedral and tetrahedral site, the estimated logfO_2 should be inbetween the $^{IV}Fe^{2+}$ and $^{VI}Fe^{3+}$ estimated fO_2 on Figure 18.

Effect of Crystal Orientation

Crystal orientation is one of the important factors affecting the Fe^{3+}/Fe_{Total} ratio measurement that did not mentioned in the Fe-XANES analysis. The Fe-XANES measurements in this study did not focus on plagioclase crystals and standard orientations, which the Fe^{3+}/Fe_{Total} ratio measurement would have a greater error bar additionally to the factors mentioned above. Dyar et al. (2001) experiment on defined oriented Fe-rich mica crystals in thin sections showed that both pre-edge and main-edge features exhibit orientation-dependant changes in both peak intensity and energy. Further experiments by Dyar et al. (2002b) on pyroxenes, amphiboles, and micas crystals with X-ray beam polarized along X, Y, and Z optical orientations drawn the same conclusion where the intensity of both pre-edge and main-edge is variable as a function of orientation. Crystal orientation contributes ±10% error in determinations of Fe^{3+}/Fe_{Total} ratio by pre-edge energy (Dyer et al., 2001, 2002b, & Abstract 5193). One way to minimize the crystal orientation error in Fe^{3+}/Fe_{Total} ratio is to orient the standard in the same way as unknown crystals (Dyar et al., 2002b).

Conclusions

Oxygen fugacity estimated on the basis of Fe^{3+} concentration in plagioclase crystals produced more oxidized values than these calculated on the basis of the Fe-Ti

oxide barometry. Many controlling factors in the magma can affect the Fe^{3+}/Fe^{2+} ratio in plagioclase crystals and their host silicate melt. Observations from this research study are summarized below.

1. Difference in timing of Fe-Ti oxide growth compared to plagioclase is likely to affect the difference between the fO_2 based on Fe-Ti oxide barometry and fO_2 based on Fe-XANES.

2. Mössbauer values provide the average of Fe^{3+}/Fe_{Total} ratio in plagioclase crystals.

3. Variation in % CaO* in the bulk compositions and An content in the plagioclase might have a large influence to fO_2 estimations. CaO increases the calculated fO_2 compared to values calculated on the basis of the Fe-Ti oxide barometry especially in the Quizapu bulk composition. This observation is supported by the conclusion of Hofmeister and Rossman (1984) that the Fe^{3+}/Fe_{Total} ratio increases in plagioclase with increasing An content. Therefore, plagioclase crystal structure has a definite influence on the $Fe^{3+}Al^{IV}_{-1}$ substitution (21). Further research is needed to determine if there is a relationship between % CaO*, An content, equation (30), and fO_2.

4. The activity of water is directly related to Fe^{3+}/Fe_{Total} ratio in the silicate melt. The effect of water needs to be added to the Kress and Carmichael empirical formula for situations with $fO_2 <$ NNO +1.

5. Pressure has an inverse relationship with Fe^{3+}/Fe_{Total} ratio in the silicate melt and also affects the water content. Pressure needs to incorporate into the Kress and Carmichael empirical formula.

6. Error bars on Fe-XANES measurements are large. The plagioclase standards that are used to calculate the linear equation (28) might not be accurate. The standard equation should be nonlinear based on the work of Wilke et al. (2001).

7. The standards and unknown crystals should be oriented in the same way to minimize the additional error during Fe-XANES measurements.

8. Calculation of fO_2 from Fe^{3+}/Fe_{Total} ratio and total FeO in plagioclase from young volcanic rocks yields fO_2 that are close to, but not identical to fO_2 calculated by Fe-Ti oxide barometry.

9. This technique may permit monitoring of small changes in fO_2 during the crystallization of single feldspar crystals.

10. Further research is needed to minimize the fO_2 marginal error between calculated values and Fe-Ti oxide barometry values.

Session	Sample Name	Wt% FeO	Wt% Fe2O3	D Fe2O3/FeO	CAFS	NAFS	Ave $fO2$	Variance of Ave $fO2$
975	msh1plagcenter.084	4.27	0.20	0.05	-14.94	-3.98	-9.77	2.02
975	msh1plagrim.085	6.27	0.19	0.03	-15.85	-4.15	-10.34	1.75
975	msh2plagcenter.086	3.21	0.11	0.03	-15.50	-4.10	-10.13	1.78
975	msh2plagrim.087	5.94	0.23	0.04	-15.33	-4.04	-10.01	1.88
975	msh3plagcenter.088	5.91	0.11	0.02	-16.84	-4.36	-10.96	1.67
975	msh3plagrim.098	5.57	0.18	0.03	-15.71	-4.13	-10.25	1.76
975	msh5plagcenter.101	4.00	0.14	0.04	-15.44	-4.08	-10.09	1.81
975	msh5plagrim.102	5.04	0.18	0.04	-15.45	-4.07	-10.09	1.82
975	msh6plagcenter.103	4.33	0.24	0.06	-14.51	-3.88	-9.50	2.33
975	msh6plagrim.104	3.96	0.24	0.06	-14.32	-3.85	-9.39	2.52
975	msh7plagcenter.105	5.60	0.17	0.03	-15.88	-4.16	-10.36	1.73
975	msh7plagrim.106	5.12	0.16	0.03	-15.84	-4.15	-10.33	1.73
975	qui1center.128	4.34	0.06	0.01	-17.70	-4.69	-8.11	1.20
975	qui1rim.129	5.95	0.05	0.01	-18.80	-4.90	-8.55	1.10
975	qui2center.130	5.70	0.09	0.02	-17.63	-4.66	-8.07	1.23
975	qui2rim.131	4.67	0.08	0.02	-17.47	-4.64	-8.01	1.26
975	qui3center.132	4.74	0.07	0.02	-17.64	-4.67	-8.08	1.22
975	qui3rim.133	4.34	0.10	0.02	-16.84	-4.51	-7.75	1.51
975	qui4center.134	3.86	0.10	0.03	-16.55	-4.46	-7.63	1.71
975	qui4rim.135	5.02	0.12	0.02	-16.78	-4.49	-7.72	1.57
975	kat1center.143	9.05	0.33	0.04	-16.28	-4.26	-10.77	1.89
975	kat1rim.144	7.52	0.34	0.05	-15.76	-4.17	-10.45	2.08
975	kat2center.145	7.81	0.23	0.03	-16.72	-4.36	-11.06	1.77
975	kat2rim.146	6.24	0.33	0.05	-15.44	-4.11	-10.25	2.25
975	kat3center.147	7.52	0.31	0.04	-15.99	-4.21	-10.60	1.96
975	kat3rim.148	8.18	0.21	0.03	-16.97	-4.41	-11.22	1.74

Table 14. Iron partition coefficient and fO_2 of the melt composition by reducing 30% Fe^{3+} from Fe-XANES high resolution measurement

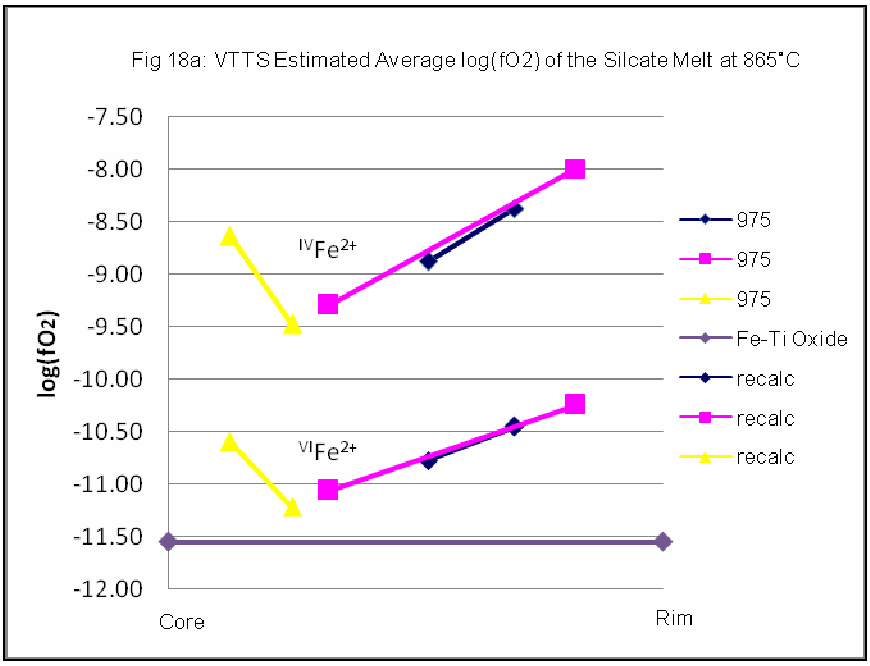
Fig 18a: VTTS Estimated Average log(fO2) of the Silcate Melt at 865°C
-7.50
-8.00
-8.50
-9.00
-9.50
-10.00
-10.50
-11.00
-11.50
-12.00
log(fO2)
IVFe2+
VIFe2+
Core
Rim
975
975
975
Fe-Ti Oxide
recalc
recalc
recalc

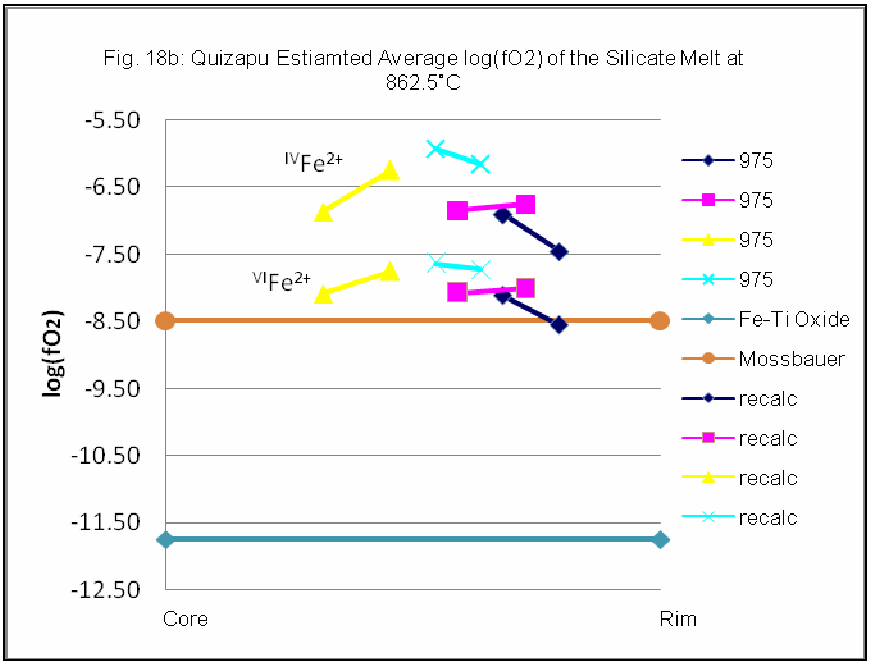
Fig. 18b: Quizapu Estiamted Average log(fO2) of the Silicate Melt at 862.5°C
-5.50
-6.50
-7.50
-8.50
-9.50
-10.50
-11.50
-12.50
log(fO2)
IVFe2+
VIFe2+
Core
Rim
975
975
975
975
Fe-Ti Oxide
Mossbauer
recalc
recalc
recalc
recalc

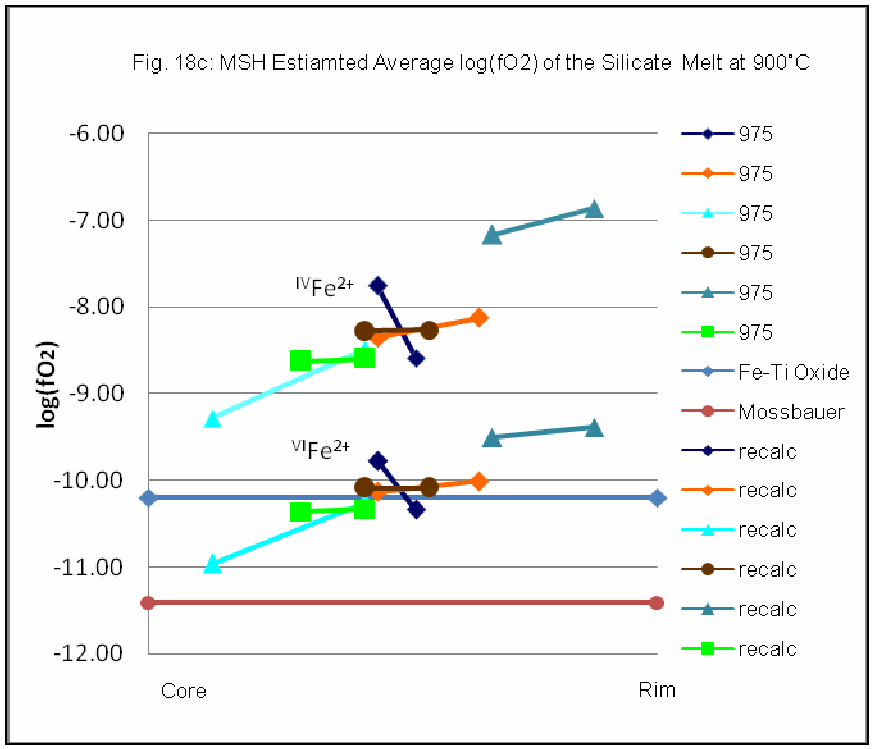

Figure 18. Recalculate estimated oxygen fugacity of the silicate melt by reducing 30% Fe^{3+} from the high resolution values on Table 6. Top estimated fO_2 pattern is from Figure 17 where the Fe^{2+} is tetrahedrally coordinated, and botton estimated fO_2 pattern is octahedrally coordinated. The recalucated averaged fO_2 produces a closer estimation to the Fe-Ti oxide barometry and Mössbauer values. a. VTTS, b. Quizapu, and c. MSH

BIBLIOGRAPHY

Adams NK, Houghton BF, Hildreth W (2006) Abrupt transitions during sustained explosive eruptions: examples from the 1912 eruption of Novarupta, Alaska. Bull Volcanol 69:189-206.

Bajt S., Sutton S.R., and Delaney J.S. (1994) X-ray microprobe analysis of iron redox states in silicates and oxides using X-ray absorption near edge structure (XANES). Geochim Cosmo Acta, 58: 5209-5214.

Baker L.L. and Rutherford M.J. (1996) The effect of dissolved water on the oxidation state of silicic melts. Geochim Cosmo Acta, 60: 2179-2187.

Blundy J. and Cashman K. (2001) Ascent-driving crystallization of dacite magma at Mount St. Helens, 1980-1986. Contrib Mineral Petrol, 140:631-650.

Blundy J. and Cashman K. (2005) Rapid decompression-driven crystallization recorded by melt inclusions from Mount St. Helens volcano. Geology, 33:793-796.

Botcharnikov, R.E., Koepke, J., Holtz, F., McCammon, C., and Wilke, M. (2005) The effect of water activity on the oxidation and structural state of Fe in a Ferro-basaltic melt. Geochim Cosmo Acta, 69: 5071-5085.

Brown G.E., Calas G., Waychunas, G.A., and petiau J. (1988) X-ray absorption spectroscopy and its applications in mineralogy and geochemistry. In Reviews in Mineralogy, 18: Spectroscopic methods in mineralogy and geology (ed. F.C. Hawrhorne). Mineralogy Socitey of America, Washington D.C., 431-512.

Burnham C.W. (1975) Water and magmas; a mixing model. Geochim Cosmo Acta, 39: 1077-1084.

Carmichael I.S.E. and Ghiorso M.S. (1986) Oxidation-reduction relations in basic magma: case for homogenious equilibira. Earth Plantet Sci Lett 78: 200-210.

Carey S. and Sigurdsson H. (1985) The May 18, 1980, eruption of Mount St. Helens, 2, Modeling of dynamics of the Plinian phase. J Geophy Res, 90:2948-2958.

Cartwright B.M. (2001) Evaluating Fe^{3+}/Fe^{2+} in plagioclase feldspars from a volcanic sucession using he microXANES Method: The Atascosa Mountains, South-central Arizona. Master Thesis, UMass Amherst.

Cashman, K. (1988) Crystallization of Mount St. Helens 1980-1986: A quantitative textural approach. Bull Volcanol, 50:194-209.

Cashman K. (1992) Groundmass crystallization of Mount St. Helens dacite, 1980-1986: a tool for interpreting shallow magmatic processes. Contrib Mineral Petrol, 109:431-449.

Cashmen K.V. and Hoblitt R.P. (2004) Magmatic precursors to the 18 May 1980 eruption of Mount St. Helens, USA. Geology, 32: 141-144.

Clowe, C.A., Popp, R.K., and Fritz, S.J. (1988) Experimental investigation of the effect of oxygen fugacity on ferric-ferrous ratios and unit-cell parameters of four natural clinoamphiboles. Am Mineral, 73: 487-499.

Coombs D.S. (1954) Ferriferrous orthoclase from Madagascar. Mineralogical Magazine, 30: 409-427.

Coombs, ML & Gardner, JE (2001) Shallow-Storage conditions for the rhyolite of the 1912 eruption at Novarupta, Alaska. Geology 29:775-778.

Crandell D.R., Mullincaux D.R., and Myer R. (1975) Mount St. Helens volcano: recent and future behavior. Science, 187:438-441.

Curtis, GH (1968) The Stratigraphy of the ejecta of the 1912 eruption of Mount Katmai and Novarupta, Alaska. Geol Soc Am Bull 72:153-210

Dickenson M.P. and Hess P.C. (1981) Redox equilibria and the structural role of iron in alumino-silicate melts. Contrib Mineral Petrol, 78: 352-357.

Dickenson M.P. and Hess P.C. (1986) The structural role and homogeneous redox equilibria of iron in peraluminous, metaluminous and peralkaline silicate melts. Contrib Mineral Petrol, 92: 207-217.

Donnadieu F. and Merle O. (2001) Geometrical constraints of the 1980 Mount St. Helens intrusion from analogue models. Geophys Res Letters, 28:639-642.

Dyar M.D., Delaney J.S., Sutton S.R., and Schaefer M.W. (1998) Fe^{3+} distribution in oxidized olivine: A synchrotron micro-XANES study. Am. Mineral, 83: 1361-1365.

Dyar M.D., Delaney J.S., and Sutton S.R. (2001) Fe XANES spectra of iron-rich micas. European J. Mineral, v.13; no.6; 1079-1098.

Dyar M.D., Lowe E.W., Guidotti C.V., and Delaney J.S. (2002a) Fe^{3+} and Fe^{2+} partitioning among silicates in metapelites: A synchrontron micro-XANES study. Am Mineral. 87: 514-522.

Dyar M.D., Gunter M.E., Delaney J.S., Lanzarotti A., and Sutton S.R. (2002b) Systematics in the structure and XANES spectra of pyroxenes, amphiboles, and micas as derived from oriented single crystals. Can Mineralogist, 40: 1375-1393.

Dyar M.D., Delaney J.S., Rossman G.R., and Sutton S.R. Polarized Fe XANES pre-edge spectroscopy of feldspars. Abstract No. Dyar5193

Eichelberger, J.C. and Izbekov, P.E. (2000) Eruption of andesite triggered by dyke injection: contrasting case at Karymsky Volcano, Kamchatka and Mt Katmai, Alaska. PhilosTran R Soc Lond 358: 1465-1485.

Faye G.H. (1969) The optical absorption spectrum of tetrahedrally bonded Fe^{3+} in orthoclase. Canadian Mineralogist, 10: 112-117.

Fierstein J and Hildretih W (1992) The plinian eruptions of 1912 at Novarupta, Katmai National Park, Alaska. Bull Volcanol 54:646-684.

Fischer R., Cottrell, E., Lanzorotti, A., and Kelley K.A. (2007) Micro-XANES determination Fe speciaton in natural basalts at mantle-relevant fO_2. American Geophysical Union, Fall Meeting, abstract DI33A-1119.

Frost R.B. (1991) Introduction to oxygen fugacity and its petrologic importance. Revs. Mineral., 25: 1-9.

Gaillard F., Scaillet B., Pichavant M., and Beny J.M. (2001) The effect of water and fO_2 on the ferric-ferrous ratio of silicic melts. Chem Geol, 174: 255-273.

Gaillard F., Pichavant M., and Scaillet B. (2003) Experimental determination of activites of FeO and Fe_2O_3 components in hydrous silicic melts under oxidizing conditions. Geochim Cosmo Acta, 67: 4389-4409.

Gardner J.E., Carey S., and Rutherford M.J. (1995) Petrologic diversity in Mount St. Helens dacite during the last 4,000 years: implications for magma mixing. Contrib Mineral Petrol, 119:224-238.

Griffen, D.T. (1992) *Silicate Crystal Chemistry*. Oxford University Press, NY.

Hamilton, D.L., Burnham, C.W., and Osborn, E.F. (1964) The stability of water and effects of oxygen fugacity and water comtent on crystallization in mafic magmas. J. Petrol. 5:21-39.

Hammer JE, Rutherford MJ, Hildreth W (2002) Magma storage prior to the 1912 eruption at Novarupta, Alaska. Contrib Mineral Petrol 144:144-162

Hildreth, W (1983) The compositionally zoned eruption of 1912 in the Valley of Ten Thousand Smokes, Katmai National Park, Alaska. J Volcanol Geotherm Res 18:1-56

Hildreth, W. & Drake, R.E. (1992) Volcán Quizapu, Chilean Andes. Bulletin of Volcan. v.54:93-125.

Hildreth, W & Friestein, J (2000) Katmai volcanic cluster and the great eruption of 1912. Geol Soci Am Bull 112:1594-1620

Hoblitt R.P. and Harmon R.S. (1993) Bimodal density distribution of cryptodome dacite from the 1980 eruption if Mount St. Helens, Washington. Bull Volcanol, 55:421-437.

Hofmeister A.M. and Rossman G.R. (1984) Determination of Fe^{3+} and Fe^{2+} concentrations in feldspar by optical absorption and EPR spectroscopy. Physics and Chemistry of Minerals, 11: 213-224.

Kilinc A., Carmicheal I.S.E., Rivers M.L., and Sack R.O. (1983) The ferric-ferrous ratio of natural silicate liquids equilibrated in air. Contrib Mineral Petrol, 83: 136-140.

King, P.L., Hervig, R.L., Holloway, J.R., Delaney, J.S., and Dyar, M.D. (2000) partitioning of Fe^{3+}/Fe_{total} between amphibole and basanitic melt as a function of oxygen fugacity. Earth Planetary Sci Letter, 178: 97-112.

Kress V.C. and Carmicheal S.E. (1988) Stiochiometry of the iron oxidation reaction in silicate melts. Am Mineral, 73: 1267-1274.

Kress V.C. and Carmicheal S.E. (1989) The lime-iron-silicate melt system: redox and volume systematics. Ceochim Cosmo Acta, 53: 2883-2892.

Kress V.C. and Carrmicheal S.E. (1991) The Compressibility of Silicate Liquids containg Fe_2O_3 and the Effect of Composition, Temperature, Oxygen Fugacity, and Pressure on Their Redox States. Contrib Mineral Petrol, 108: 82-92.

Kuroda, Y., Hariya, Y., Suzuoki, T., and Matsuo, S. (1975) Pressure effect on water content of amphiboles. Geophys Res Lett, 2: 529-531.

Longhi, J., Walker, D., and Hays, J.F. (1976) Fe and Mg in plagioclase. In: Proc Lunar Sci Conf 7th, pp 1281-1300.

Lowenstern, JB (1993) Evidence for a copper-bearing fluid in magma erupted at the Valley of Ten Thousand Smokes, Alaska. Contrib Mineral Petrol 114:409-421

Lundgaard, K.L. and Tegner, C. (2004) Partitioning of ferric and ferrous iron between plagioclase and silicate melt. Contrib Mineral petrol, 147: 470-483.

Merzbacher, C. & Eggler, D.H. (1984) A magmatic geohygrometer: applications to Mount St. Helens and other dacitic magmas. Geology 12:587-590.

Moore G., Vennemann T., and Carmicheal I.S.E. (1995) Solubility of water in magmas to 2 kbar. Geology, 23:1099-1102.

Mysen B.O., Virgo D., Harrison, W.J., and Scarfe C.M. (1980) Solubility mechanisms of H_2O in silicate melts at high pressures and temperatures: a Raman spectroscopic study. Am Mineral, 65: 900-914.

Mo X., Carmichael I.S.E., Rivers M., and Stebbins J. (1982) The partial molar volume of Fe_2O_3 in multicomponent silicate liquids and the pressure dependence of oxygen fugacity in magmas. Mineral Mag 45: 237-245.

Moore M., Righter K., and Carmicheal I.S.E. (1995) The effect of dissolved water on the oxidation state of iron in natural silicate liquids. Contrib Mineral Petrol, 120: 170-179.

Mullineaux D.R., Hyde J., and Rubin M. (1975) Widespread late glacial and postglacial tephra deposits from Mount St. Helens volcano, Washington. J Res US Geol Surv, 3:329-335.

Pallister, J.S., Hoblitt, R.P., Crandell D.R., Mullineoux, D.R. (1992) Mount St. Helens a decade after the 1980 eruptions: magmatic models, chemical cycles, and a revised hazards assessment. Bull Volcanol, 54:126-146.

Philpotts, A.R. (1990) *Principles of Igneous Petrology.* Prentice Hall: New Jersey, p. 498

Phinney, W.C. (1992) Partition coefficients for iron between plagioclase and basalt as a function of oxygen fugacity: Implications for Archean and lumar anorthosites. Geochim Cosmo Acta, 56: 1885-1895.

Popp, R.K., Virgo, D., Yoder Jr., H.S., Hoering, T.C., and Phillips, M.W. (1995) An experimental study of phase equilibria and Fe oxy-component in kaersutitic amphibole: Implications for the f_{H2} and a_{H2O} in the upper mantle. Am Mineral, 80: 534-548.

Redhammer G.J., Beran A., Dachs E., and Amthauer G. (1993) A Mössbauer and X-Ray diffraction study of annites synthesized at different oxygen fugacities and crystal chemical implications. Phys Chem Minerals, 20: 382-394.

Rutherford M.D., Sigurdsson H., Carey S., and Davis A. (1985) The May 18, 1980 eruption of Mount St. Helens. 1. Melt composition and experimental phase equilibria. J Geophys Res, 90:2929-2947.

Rutherford M.J. and Devine J.D. (1988) The May 18, 1980 eruption of Mount St. Helens. 3. Stability and chemistry of amphibole in the magma chamber. J Geophys Res, 93:11949-11959.

Rutherford M.J. and Hill P.M. (1993) Magma ascent rates from amphibole breakdown: an experimental study applied to the 1980-1986 Mount St. Helens eruption. J Geophy Res, 98:19667-19686.

Sack R.O., Carmicheal I.S.E., Rivers M., and Ghiorso M.S. (1980) Ferric-ferrous equilibria in natural silicate liquids at 1 bar. Contrib Mineral Petrol, 75: 369-376.

Scala C.M., Hutton D.R., and mclaren A.C. (1978) NMR and EPR studies of some chemically intermediate plagioclase feldspars. Physics and Chemistry of Minerals, 3: 33-44.

Stewart b., Walker G.W., Wright T.L., and Fahey J.J. (1966) Physical properties of calcic labradorite from lake County, Oregon. Am Mineral, 51: 177-197.

Stolper E. (1982) Water in silicate Glasses: An infrared spectroscopic study. Contrib Mineral Petrol, 81: 1-17.

Stolper E. (1989) Temperature dependence of the speciation of water in rhyolitic melts and glasses. Am Mineral, 74: 1247-1257.

Sugawara, T. (2000) Thermodynamic analysis of Fe and Mg partitioning between plagioclase and silicate liquid. Contrib. Mineral. Petrol., 138, 101-113.

Sugawara, T. (2001) Ferric iron partitioning between plagioclase ansd silicate liquid; thermodynamics and petrological applications. Contrib. Mineral. Petrol., 141: 659-686.

Sykes D. and Kubicki J.D. (1993) A model for H_2O solbility mechanisms in albite melts from infrared spectroscopy and molecular orbital calculations. Geochim Cosmo Acta, 57: 1039-1052.

Wilke, M., Farges, F., Petit, P.E., Brown Jr., G.E., and Martin, F. (2001) Oxidation state and coordination of Fe min minerals: An Fe K-XANES spectroscopic study. Am Mineral, 86:714-730.

Mount St. Helens image taken in 1994 by NASA and later added details by Lyn Topinka from wikipeida website. (http://en.wikipedia.org/wiki/Mount_St._Helens)